The Astrophysical Journal, 844:155 (17pp), 2017 August 1 https://doi.org/10.3847/1538-4357/aa7b30

Attenuation Modified by DIG and Dust as Seen in M31

Neven Tomičić[1], Kathryn Kreckel[1], Brent Groves[2], Eva Schinnerer[1], Karin Sandstrom[3], Maria Kapala[4], Guillermo A. Blanc[5,6,7], and Adam Leroy[8]
[1] Max Planck Institute for Astronomy (MPIA), Königstuhl 17, 69117 Heidelberg, Germany; tomicic@mpia-hd.mpg.de
[2] School of Astronomy and Astrophysics, Australian National University, Canberra, ACT 2611, Australia
[3] Center for Astrophysics and Space Sciences, Department of Physics, University of California, San Diego, 9500 Gilman Drive, La Jolla, CA 92093, USA
[4] Department of Astronomy, University of Cape Town, Republic of South Africa
[5] Observatories of the Carnegie Institution for Science, 813 Santa Barbara Street, Pasadena, CA 91101, USA
[6] Departamento de Astronomía, Universidad de Chile, Camino del Observatorio 1515, Las Condes, Santiago, Chile
[7] Centro de Astrofsica y Tecnologías Afines (CATA), Camino del Observatorio 1515, Las Condes, Santiago, Chile
[8] Department of Astronomy, The Ohio State University, 140 West 18th Avenue, Columbus, OH 43210
Received 2016 December 21; revised 2017 June 19; accepted 2017 June 20; published 2017 August 2

Abstract

The spatial distribution of dust in galaxies affects the global attenuation, and hence inferred properties, of galaxies. We trace the spatial distribution of dust in five approximately kiloparsec fields of M31 by comparing optical attenuation with the total dust mass distribution. We measure the attenuation from the Balmer decrement using Integral Field Spectroscopy and the dust mass from *Herschel* far-IR observations. Our results show that M31's dust attenuation closely follows a foreground screen model, contrary to what was previously found in other nearby galaxies. By smoothing the M31 data, we find that spatial resolution is not the cause for this difference. Based on the emission-line ratios and two simple models, we conclude that previous models of dust/gas geometry need to include a weakly or non-attenuated diffuse ionized gas (DIG) component. Due to the variation of dust and DIG scale heights with galactic radius, we conclude that different locations in galaxies will have different vertical distributions of gas and dust and therefore different measured attenuation. The difference between our result in M31 with that found in other nearby galaxies can be explained by our fields in M31 lying at larger galactic radii than the previous studies that focused on the centers of galaxies.

Key words: dust, extinction – galaxies: individual (M31) – galaxies: ISM – H II regions

1. Introduction

The attenuation and reddening by dust can severely impair our understanding of galaxies and the ISM environment. Dust preferentially absorbs ultraviolet (UV) and optical photons and re-emits this radiation in the infrared (IR). The final impact of this reprocessing on the spectral energy distribution (SED) of a galaxy is dependent upon the properties of the dust and its spatial distribution relative to the stars and gas (Witt et al. 1992; Gordon et al. 2003; Draine 2011b). To understand the observed light from the galaxies, correct models of dust properties, distribution, and the resulting effect on the spectra are needed.

Extinction is the result of absorption and scattering of the light by dust along a single line of sight. The effect is more pronounced on light at shorter wavelengths, resulting in an overall reddening of the light (usually denoted by the selective extinction E_{B-V}). With different dust/gas geometrical distribution, the effects on observed light would be different. The combined effects of extinction and geometry is usually called "attenuation." Caplan & Deharveng (1986), Witt et al. (1992), Calzetti et al. (1994), Gordon et al. (2003), and Draine (2011a) derived various models for the relative dust/gas distributions and the corresponding effects on the stellar light and observed attenuation. Among these models, two show extreme scenarios, where in one the dust and gas are not mixed and in another they are.

The "foreground screen" model assumes that the dust is distributed as a thin screen between the stars and the observer. This model represents the "Extinction" case where all light is either absorbed or scattered out of the line of sight, and A_V correlates linearly with dust mass surface density. However, if the dust screen is on the far side behind the stars compared to the observer, that will result in no extinction.

The "mixed media" model assumes the stars and dust are uniformly distributed and mixed. In this distribution, some stars suffer relatively less extinction than others (i.e., closer to the observer), altering the attenuation. Also, in this distribution, light from stars can be scattered into the line of sight of the observer, also altering the attenuation.

van der Hulst et al. (1988) and Calzetti et al. (1996) observed ratios of various hydrogen lines in 14 nearby galaxies. They found that integrated approximately kiloparsec regions in these galaxies typically had attenuations suggesting a dust distribution between the screen and mixed models.

Liu et al. (2013) investigated the dust attenuation of H II regions in M83 using the ratio of the Balmer and Paschen lines from *Hubble Space Telescope*/WFC3 narrow-band imaging at ∼6 pc spatial resolution. They found a diverse range of geometries, where the center of M83 has a dust distribution closer to the mixed model while the outer radii have H II regions with attenuation closer to the screen model. When averaged to ⩾100–200 pc spatial resolution, their data follow a foreground screen model.

Using optically thin tracers, one simple way of deducing the spatial distribution of dust is to observe the effect of extinction on the known ratio of optical Balmer lines (Hα, Hβ, Hγ, Hδ) and then compare it with the extinction expected from the dust mass distribution.

While previous works of van der Hulst et al. (1988), Calzetti et al. (1996), and Liu et al. (2013) used only attenuation based on optical and near-infrared (NIR) lines to determine the dust

distribution, Kreckel et al. (2013; hereafter K13) used two independent measures of dust—optical attenuation and IR emission—to measure the distribution. In K13, eight nearby galaxies were observed as part of the KINGFISH[9] project (Kennicutt et al. 2011) with optical integral field spectroscopy (IFS) and far-IR (FIR) observations (done with the *Herschel Space Observatory*; Griffin et al. 2010; Pilbratt et al. 2010). They distinguish features at physical scales of ∼1 kpc within the galaxy disks. K13 conclude that the distribution of dust and gas in these galaxies lies somewhere between the screen and mixed models.

Following the methodology of K13, we observed five fields in the Andromeda galaxy (M31) to determine the spatial distribution of dust as compared to the ionized gas at high spatial resolution (≈100 pc or 24.″9). Compared to K13, our higher resolution gives us the opportunity to resolve star-forming complexes at ≈100 pc resolution and H II regions at the ≈10 pc resolution. With this resolution, we are able to trace different environments of dust and ionizing gas. We analyze the dust distribution using two extreme dust models (foreground screen and mixed model) and compare our results with those from K13.

The Andromeda galaxy is the closest large spiral galaxy, providing the opportunity to observe dust on physically smaller scales than those in K13. M31 is a massive ($\sim 10^{10.5}\ M_{\odot}$) SA(s)b galaxy with ring-like structures. Its distance from the Milky Way is ∼780 kpc (Stanek & Garnavich 1998) and it is highly inclined (∼70°, Dalcanton et al. 2012). R_{25} of M31 is ≈20.5 kpc (Zurita & Bresolin 2012). The total star-formation rate (SFR) for the entire disk of M31 is $\sim 1\ M_{\odot}\ \mathrm{yr}^{-1}$ (Williams 2003; Lewis et al. 2015).

In this article, Section 2 presents an overview of the data and its reduction details. In Section 3, we show our main results and a comparison between the attenuation and dust mass column density. In Section 4, we discuss possible explanations of our results. The conclusions are presented in Section 5, followed by a summary.

2. Data

The Andromeda Galaxy (M31) provides the best compromise between spatial resolution and a global view in the study of galaxy structure. The proximity of M31 to the Milky Way enables the observation of its ISM with high resolution (∼10.2 pc in the optical and ∼100 pc at 350 μm).

To study the relationship between attenuation and dust in M31, we have combined optical integral field unit (IFU) spectroscopy with far-infrared imaging. The attenuation is traced using optical spectroscopy, and the dust mass surface density was independently derived from FIR SED fitting using *Herschel* and *Spitzer* (*Spitzer Space Telescope*) photometry.

We targeted five fields in M31, chosen to have a large suite of ancillary multiwavelength data (Hα, 24 μm and FUV) and to cover a range of SFRs and environments. The fields and data are also used by Kapala et al. (2015) to trace the origin of [C II] line emission, as part of the Survey of Lines in M31 (SLIM, PI Sandstrom K.). The positions of the five fields are shown in Figure 1 and Table 1.

In the following subsections, we describe the data reduction, flux calibration, and analysis of the spectra that are performed following the procedures outlined in K13 and Kapala et al. (2015).

[9] Key Insight on Nearby Galaxies: A Far-infrared Survey with *Herschel*.

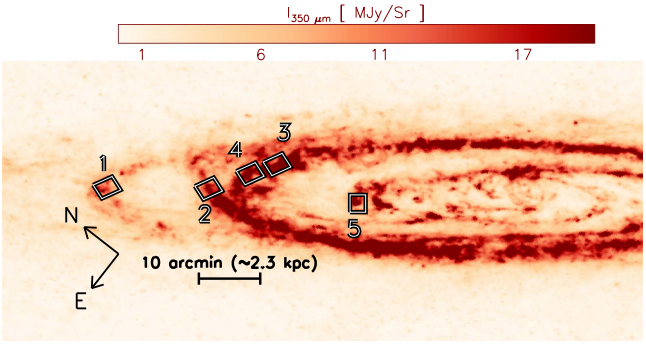

Figure 1. Positions of the five fields in M31 used in this work, overlaid on a *Herschel* SPIRE 350 μm intensity map in 24.″9 resolution.

Table 1
Coordinates and Approximate Distances[a] from the Galaxy Center (in kpc) for Our Fields

Field	R.A. (J2000)	Decl. (J2000)	R (kpc)
1	$00^{h}46^{m}28.^{s}88$	+42°11′38.″16	16
2	$00^{h}45^{m}34.^{s}04$	+41°58′33.″53	12.2
3	$00^{h}44^{m}36.^{s}04$	+41°52′53.″58	11.7
4	$00^{h}44^{m}58.^{s}54$	+41°55′09.″14	11.8
5	$00^{h}44^{m}25.^{s}58$	+41°37′37.″20	6.8

Note.
[a] R_{25} of M31 is ≈20.5 kpc (Zurita & Bresolin 2012).

2.1. Optical IFS

We observed all fields using the Potsdam Multi-aperture Spectrophotometer (Roth et al. 2005) at the 3.5 m telescope at the Calar Alto Observatory on 2011 September 16–24. To split the spatial image, the telescope uses a specialized fiber-bundle, PPaK, which consists of 331 bare science fibers (with an additional 36 sky and 15 calibration fibers) in a hexagonal grid. The grid has a diameter of 75″ (Verheijen et al. 2004) and spatial sampling of 2.″7 per fiber. We used the 4 k × 4 k CCD detector with the V300 grating to achieve a wavelength coverage of 3500–9000 Å (centered at 5400 Å) and resolution of $R = 1000$.

Each of the five observed fields combines 10 pointings in a mosaic, resulting in an area of 3′ × 4′ (680 pc × 900 pc) for each field. Resulting mosaics have an effective PPaK resolution of 2.″7. Each pointing was observed with a dither pattern (three dither positions shifted by Δdecl. = +1.″56, Δdecl. = +0.″78, and ΔR.A. = +1.″56, ΔR.A. = −0.″78) with 2 × 600 s exposures in order to fill in gaps between the fibers, thus covering the entire field of view. Dedicated sky observations (with 120 s exposures) were taken in the same manner between each science observation in order to be subtracted later during calibration.

Astrometry for each mosaic position was applied by eye through comparison of compact H II regions with Hα images from the Local Group Galaxies Survey (Azimlu et al. 2011). Additionally, we compared r- and g-band SDSS images with our data by applying the SDSS response functions for the corresponding bands to our observed spectra. Maximum deviation in astrometry are 2″, with a mean offset of around 1″.

Astrometric inaccuracies at this level do not affect our data analysis because we compare the A_V and dust maps at 25″ resolution.

To translate the electron count values into fluxes, we observed the standard stars BD +33d2642 and BD +25d4655 (Oke 1990). The positions of lines and spectra on the detector, the optical path and the transmission are all affected by fiber flexure of the IFU instrument (Sánchez 2006). To correct for these effects, we obtained calibration continuum lamp images (used for positioning of the spectra), He+HgCd arc lamp images (used for wavelengths calibration) and twilight flats (used for accurate flat fielding).

The atmospheric conditions were mostly clear, resulting in approximately uniform imaging of our fields. The observations of some pointings were repeated on September 24th due to bad weather (clouds) or moonlight contamination. Seeing was subfiber (less than 2.″7) for all observations.

2.1.1. Calibration

We reduce and calibrate all the data using the P3D software package,[10] version 2.2.6. (Sandin et al. 2010). For the first step, we perform a bias correction using the median image of all bias frames as a master bias. Next, we obtain a master flat field from all twilight flat images. Observations are cleaned of cosmic rays following the L.A. Cosmic technique (van Dokkum 2001) as adapted within P3D. We verify that the cosmic-ray removal algorithm implemented in P3D robustly cleans up the images and the corresponding noise maps. We then create the master trace mask to determine the position of all spectra on the CCD. The trace mask is constructed by stacking multiple calibration continuum lamp images, and fitting the peaks of emission lines with Gaussian functions along the cross-dispersion axis (Sandin et al. 2010). To remove the possibility of overlapping Gaussians, a modified optimal extraction method is applied (Horne 1986) that simultaneously fits all the line profiles. The He+HgCd arc lamp images are used for construction of the dispersion mask, which calculates positions for all wavelength bins along the dispersion axis (Sandin et al. 2010). Furthermore, to remove instrumental scattered light from the CCD detector, we remove the spectra, interpolate the flux of the remaining background, and remove it from the raw spectra. We absolute flux calibrate all the data using a spectral response function calculated by comparing the observed stellar spectrum of the standard star and the spectrum from the Oke (1990) catalog of the corresponding star. The sky-subtracted stellar spectra is derived from the sum of fibers containing flux from the standard star BD +33d2642.

2.1.2. Sky Subtraction, Relative Flux Calibration, and Data Cubes

The P3D package reduces the PPaK observations into calibrated row-stacked spectrum (RSS) images, from which we then subtract the sky contamination and flux-calibrate them.

Due to the large spatial extent of M31 on the sky, none of the sky fibers, observed simultaneously with the field of view, could be used for sky subtraction. Dedicated sky fields were observed before and after every science field with 120 s exposure times. The sky fields are processed following the same procedure as our science fields. We extract one median sky spectrum for each pointing of sky field observation and we linearly interpolate between sky exposures made before and after each science observations. Such a simple interpolation is possible because the majority of sky emission features change slowly with time. Because not all observing conditions were photometric and some observations ended during twilight, this interpolation technique failed for 23 of the pointings (out of a total of 50 pointings). In these cases, we assume that the median science spectrum across the field does not change significantly between dither positions. We calculate a sky-subtracted median of the science observation closest to the sky observation that appears least contaminated by clouds or twilight. Then we subtract this median science spectrum from the median observed spectrum in the remaining dither positions to recover a single sky spectrum. Finally, we subtract this sky spectrum from each individual fiber spectrum in that dither position.

To relative flux calibrate the RSS spectra, we compare them with Sloan Digital Sky Survey (SDSS, York et al. 2000) images of the same area (Tempel et al. 2011). We use the positions and sizes of all fibers, apply the SDSS response functions to the spectra, and compare resulting photometric fluxes with SDSS g- and r-band images. Then we scale each dither and combine them into pointings.

The final step was to combine the now flux-calibrated and sky-subtracted RSS spectra for all pointings into a single 3D spectral data cube. To do this we combine each of the spectra onto a grid of 1 arcsec^2 spaxels using a Delaunay linear triangulation (Delaunay 1934) individually for each wavelength. Errors from the data and sky contribution (calculated by P3D) are propagated through the entire calibration process.

2.1.3. Line Maps

The optical galaxy spectrum contains both stellar spectra (with continuum, emission, and absorption lines) and emission lines from the ionized gas. We separate the nebular emission from the stellar spectra using the GANDALF[11] software package[12] version 1.5 (Sarzi et al. 2006). GANDALF simultaneously fits both the emission lines and stellar continuum in an iterative approach.

It fits the emission lines using the penalized pixel-fitting method (pPXF; Cappellari & Emsellem 2004). Each prominent emission line is fit by a Gaussian profile with the kinematics tied together (i.e., v and σ) but fluxes left free. To fit the stellar continuum, we use template spectra taken from the Tremonti et al. (2004) library of Bruzual & Charlot (2003) simple stellar population (SSP) templates for a range of stellar ages (100 Myr to 12 Gyr) and metallicities ($Z = 0.004$ and 0.05). While SSP spectra may not represent the resolved stellar populations in our fields in M31, we chose to use the same templates as K13 for consistency. All templates are convolved to match the spectral resolution of our spectra.

We checked if using other SSP templates or stellar spectra (with higher spectral resolution and different stellar populations) could change the results of our fitting and alter the underlying stellar absorption features. We used the MILES SSP and stellar spectra library templates (Sánchez-Blázquez et al. 2006; Falcón-Barroso et al. 2011) in fitting our spectra and found that the results do not show any significant difference compared to using the Tremonti et al. (2004) library.

[10] http://p3d.sourceforge.net/

[11] Gas and Absorption Line Fitting.

[12] http://www-astro.physics.ox.ac.uk/~mxc/software/

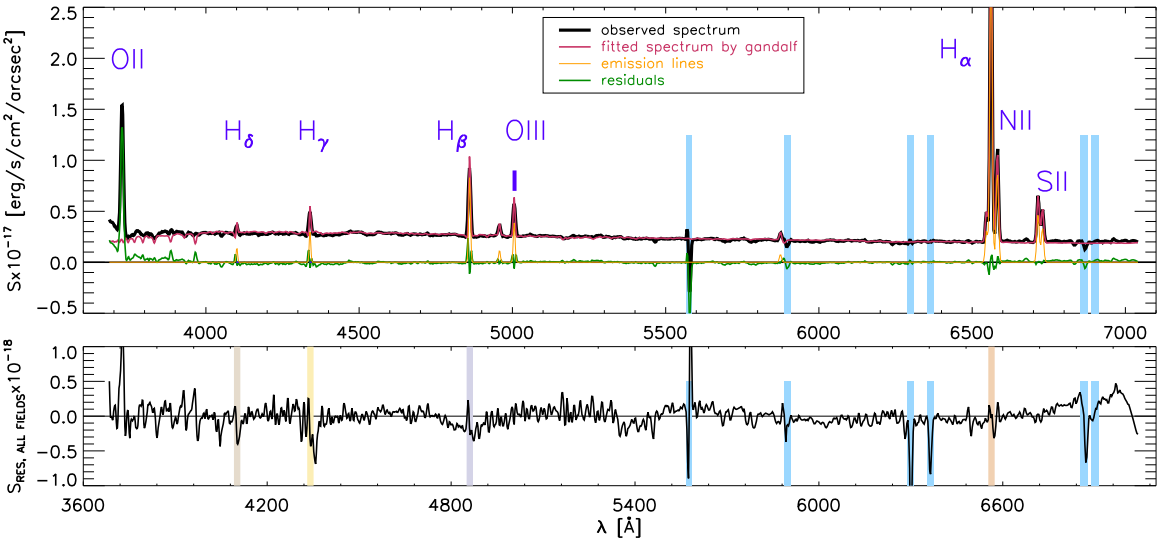

Figure 2. Upper panel—example GANDALF spectrum fit for one spaxel in Field 1. The black line is the original scientific spectrum, the red line is the fitted spectrum (including continuum and emission lines), the yellow lines show just the emission lines and the green line shows the fit residuals. Bright emission lines are labeled, while bright omitted sky lines are shaded in blue. Note that the [O II]λ 3727 emission-line doublet is not fit with the other lines (see the text for details). Lower panel—stacked residuals of all fields. Filled, colored areas indicate the positions of Balmer lines, while the bright sky lines are shaded in blue.

In fitting the continuum, we also allow for a multiplicative third-order Legendre polynomial correction. This correction is necessary due to the poor flat-field correction in the blue part of the spectra caused by low CCD sensitivity, and to allow for stellar continuum attenuation by dust intrinsic to the fields of M31.

Foreground extinction from the Milky Way is also accounted for in the spectral fitting. However, this is considered to be uniform across the disk of M31 with an $A_V = 0.1705$ mag in all fields (based on Schlegel et al. 1998 and Schlafly & Finkbeiner 2011).

The final data products from our fitting for each spaxel in our data cubes are pure stellar continuum spectrum and fractional contribution of various SSP templates; multiplicative polynomial indicative of the intrinsic dust attenuation (and flat-field corrections); gas velocity and gas velocity dispersion; and finally individual line amplitudes and fluxes for the most prominent emission lines. Identified emission lines are Hδ, Hγ, Hβ, [O III]λ4959 Å, [O III]λ5007 Å, [N II]λ6548 Å, Hα, [N II] λ6583 Å, [S II]λ6717 Å, and [S II]λ6731 Å.

Atmospheric optical emission lines (dominant around 5500 Å) can cause problems with the sky subtraction. There is a weak Hg I 4358.34 Å sky line (Osterbrock & Martel 1992; Slanger et al. 2000) near the Hγ line, which can also affect sky subtraction and fitting of the Balmer emission line. This effect is visible in the residuals near Hγ (Figure 2, seen as an absorption feature). Additional contaminants like earthshine and zodiacal light are removed from the spectra during sky subtraction because they exist as faint, extended features on the sky and in the sky spectrum (Reach 1997). Geocoronal emission lines, spatially extended and slowly changing with time, are removed by sky subtraction and do not have a significant effect on our Balmer line fluxes due to their narrowness (Nossal et al. 2001; Haffner et al. 2003; Bishop et al. 2004).

While the [O II] λ3727 Å line doublet is detected in many of our spectra, the line is strongly affected by the poor sensitivity and subsequent calibration in the blue part of the spectrum, and hence it was not used in our analysis. Foreground stars (approximately 2–5 spaxels per field) were not removed from our data cubes, but spaxels affected by the stars are masked during our GANDALF spectral analysis.

The median 3σ sensitivities of Hα and Hβ in all fields are 7.6×10^{-18} and 4.9×10^{-18} erg s^{-1} cm^{-2} arcsec^{-2}, respectively. However, averaged or median 3σ sensitivities of Balmer lines do not determine whether the data from spaxels will be shown or excluded from the following diagrams and measurements. Data are included only if a line's amplitude is above the 3σ noise on the continuum. GANDALF calculates the noise on the continuum as the standard deviation of the residuals for the entire wavelength range, while uncertainties in the line fits as the amplitude over noise values (AoNs; Sarzi et al. 2006). Figure 2 presents an example of the spectrum fitting for one spaxel in Field 1.

2.2. FIR Data and Dust Column Densities

FIR emission is a good tracer of the amount of the dust in the line of sight (Wynn-Williams 1982; Neugebauer et al. 1984). Therefore, we use the FIR data observed by the PACS and SPIRE camera on the ESA *Herschel Space Observatory* (Griffin et al. 2010; Pilbratt et al. 2010). The dust mass surface density map of M31 presented by Draine et al. (2014), used for the comparison with attenuation maps, was determined by fitting the SED of the near and FIR emission (Groves et al. 2012) with the Draine & Li (2007) dust model. The Draine & Li (2007) model specifies the dust characteristics, like the distribution of grain sizes, the frequency-dependent opacity, the fraction of dust in polycyclic aromatic hydrocarbons (PAHs), and the dust column densities. The models were determined by calculating emission spectra (in near-IR, FIR, and sub-millimeter) and reproducing extinction curves for different abundances of small PAHs and various dust mixtures heated by different starlight intensities.

The resulting dust mass surface density map ($\Sigma_{\rm dust}$) has an effective 24.″9 Gaussian PSF (matched to SPIRE 350 μm resolution). In order to compare our final attenuation maps with the dust mass surface density maps, we convolved our cubes from the effective PPaK resolution of 2.″7 into the SPIRE 24.″9

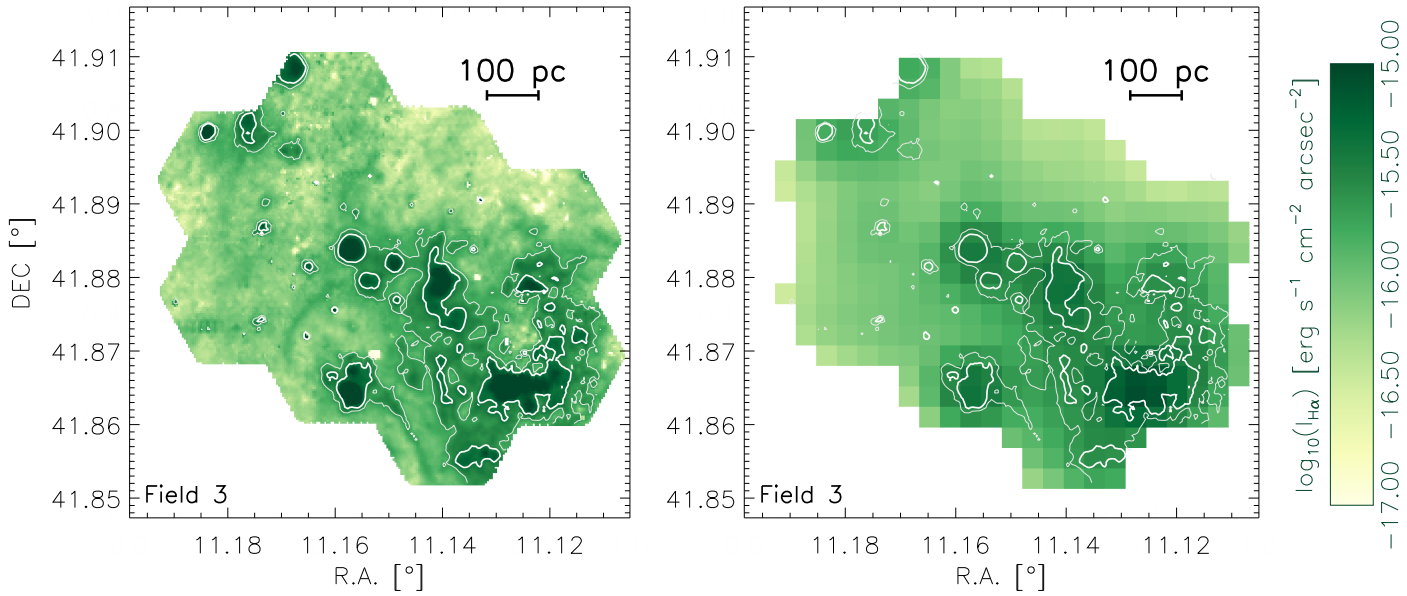

Figure 3. Example of convolving the Hα intensity images using Field 3. On the left is the un-convolved image at the native PPaK resolution of 2.″7. Contours represent the Hα intensities of 1.5×10^{-16} (thin) and 3×10^{-16} (thick) erg s^{-1} cm^{-2} arcsec^{-2}. Flux from filamentary diffuse ionized gas can be clearly seen, spanning the area between H II regions. On the right is the convolved image at the SPIRE 350 μm, 25″ resolution. Due to the increased S/N in the convolved images, some areas that are not robustly detected in the native images are included in the convolved ones (see the white contours in the Field). These features are not significant in the native map, yet clear emission lines are seen in every spaxel in the convolved image.

resolution. To convolve the data we use the kernels and the routine described in Aniano et al. (2011).

We convolve the data cubes by splitting them into images for each wavelength bin, and convolving each image separately. Before the convolution process, we add extrapolated values to the area outside the edges of the image, convolve the image, and then replace those areas with blanks after the process. Then we reassemble the cubes to the SPIRE 350 μm image grid in order to compare the maps. After the convolution, we perform the same fitting routine and spectral analysis on the convolved images as described in Section 2.1.3.

This convolution technique changes the Balmer lines intensities (up to 30%) on the edges of the data cubes, depending on the position of bright H II regions. It affects both Balmer lines simultaneously, which results in only small changes in A_V. If we compare A_V maps derived from the convolved data cubes and smoothed (but not convolved) cube, changes in A_V can be up to 0.3 mag for the bright regions. The effects of foreground stars are minimized due to the convolution process. Figure 3 shows an example of our un-convolved and convolved maps of Hα emission within Field 3.

3. Results

With the resulting data cubes and analyzed spectra, we measure the optical attenuation (A_V) and compare it with the dust mass surface density (Σ_{dust}). In the following subsections, we describe the calculation of A_V, show the resulting maps and compare the A_V and Σ_{dust} maps.

3.1. Attenuation Maps

Due to reddening by dust (correlated with the extinction) the Balmer line ratios (known as Balmer decrements) are altered from their intrinsic ratios. The total V-band extinction (A_V) is related to nebular reddening E_{B-V} by

$$A_V \equiv R_V E_{B-V}, \quad (1)$$

where R_V is the selective extinction. R_V depends on the physical characteristics of the extinguishing dust grains. In the diffuse ISM of the Milky Way, R_V has an average value of 3.1, which is the value typically assumed for massive star-forming galaxies (Schultz & Wiemer 1975; Cardelli et al. 1989; Calzetti et al. 2000). We assume the same R_V value for M31 because our fields are at similar galactic radii as the Sun (at 0.3–0.6 R_{25}; Bigiel & Blitz 2012) and with similar metallicities (Zurita & Bresolin 2012; Draine et al. 2014). The reddening between two lines (F_1 and F_2) is calculated as (Calzetti et al. 1994)

$$E_{B-V} = \frac{2.5}{k_2 - k_1} \log_{10}\left(\frac{F_1/F_2}{R_{int}}\right), \quad (2)$$

where k is the extinction as a function of wavelength for the corresponding lines. Here we use the extinction curve from Cardelli et al. (1989). By using the Calzetti et al. (2000) attenuation curve instead, the resulting inferred A_V would decrease by 9%. That systematic shift should be kept in mind when comparing our results with those found by K13, where they used the Calzetti et al. (2000) curve. The difference between those two curves is because the Cardelli et al. (1989) curve solely accounts for foreground extinction, while the Calzetti et al. (2000) curve takes into account geometrical effects on attenuation.

We assume an intrinsic flux ratio of $R_{int} = H\alpha/H\beta = 2.86$, corresponding to an ionized gas temperature of $T \approx 10^4$ (assuming case B recombination; Miller 1974; Osterbrock 1974; Osterbrock & Martel 1992, 2006).

We show attenuation (A_V) maps and the dust mass surface density maps (Σ_{dust}) in Figures 4 and 5. For all our fields, contours show the Hα intensities, tracing the position of the H II regions. All maps are at the same scales, which offers a direct comparison between the fields. A_V spans values between 1.5 and 4.5 mag in our fields. Similar results are observed by

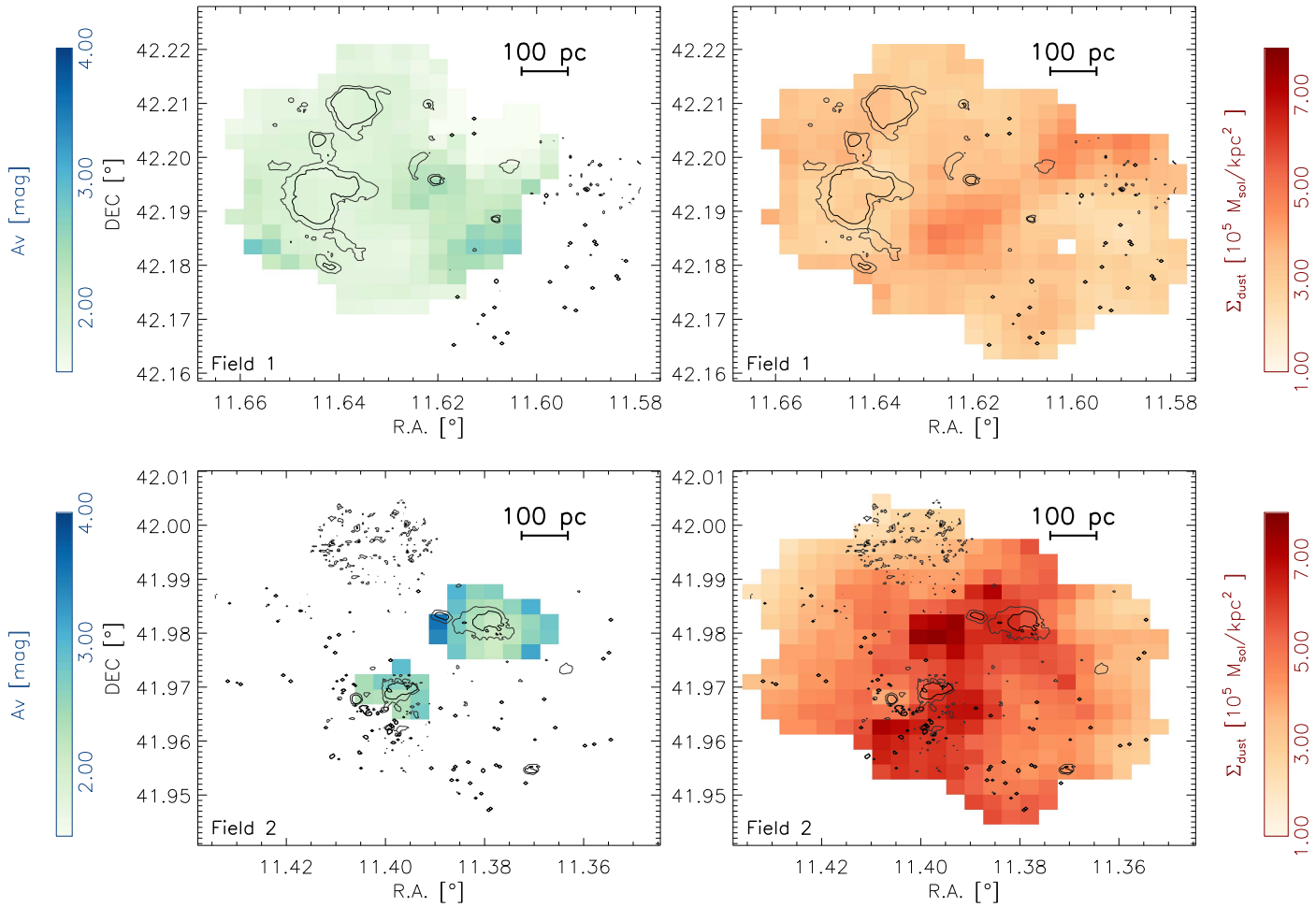

Figure 4. Attenuation (A_V, left) and dust mass surface density maps (Σ_{dust}, right) for Fields 1 (top) and 2 (bottom). Black contours represent the Hα intensities of 1.5×10^{-16} (thin) and 3×10^{-16} (thick) erg s^{-1} cm^{-2} arcsec^{-2}. Only spaxels with AoN of Balmer lines greater than three are shown. All maps are at the same scale, allowing for direct comparison between the fields. Field 1 has more uniform attenuation throughout the field. Similarly, that is matched by a uniform dust distribution that has a lower surface density compared to the other fields. One noticeable feature for Field 1 as compared to the other fields is the slight anti-correlation between the positions of the H II regions and dust.

Sanders & Caldwell (2012), where observed H II regions in M31 show values between 1 and 5 mag. The fact that there are no M31 data points with attenuation lower than $A_V = 1$ is an effect of targeting dense spiral arm regions in M31, which biases us to regions of high Σ_{dust}. If our fields were larger and included less dusty regions, we would expect our maps to have more data points with $A_V < 1$.

In general, we find that the H II regions are situated near or in the regions of higher dust mass surface densities. This is expected if the dust traces the regions of high gas density where new stars are formed. Contrary to other fields, in Field 1, the H II regions are situated in less attenuated and less dusty areas. We explain this as an effect of stellar feedback from more evolved H II regions that have already destroyed the dusty birth cloud.

We exclude from the following analysis and map regions where the Balmer lines do not exceed a threshold of AoN $\gtrsim 3$ (corresponding to S/N $\gtrsim 3$). Due to the low flux and hence S/N of the emission in Field 5, there are few spaxels that exceed this threshold. This causes some statistical difficulties in the analysis of this field. There is also a possibility that a young H II region is buried in the dense cloud, seen in the center of Field 5 (Figure 5).

Our calculated attenuation depends on the physical condition of the ionized gas (which can cause different intrinsic line ratios) and on the dust composition (resulting in different values of R_V), both of which affect the extinction curve. Therefore, the attenuation values of some data points can be different due to intrinsically different physical conditions in those regions. However, these effects are presumed to be small relative to the real variation in A_V due to the dust distribution.

3.2. A_V versus Σ_{dust}

The main goal of this paper is to compare the dust in M31 as determined via two independent methods; the attenuation derived from the Balmer decrement, and the dust mass surface density derived from IR photometry. This follows on from the work of K13 who found a relation between these measures within eight nearby galaxies, but with large scatter between galaxies.

The dust attenuation and dust mass surface density are connected via the distribution of dust. We consider here two simplistic models of the dust distribution, derived from Caplan & Deharveng (1986) and Calzetti et al. (1994). The Calzetti models predict the correlation between attenuation and the dust mass surface density for five different spatial distributions of

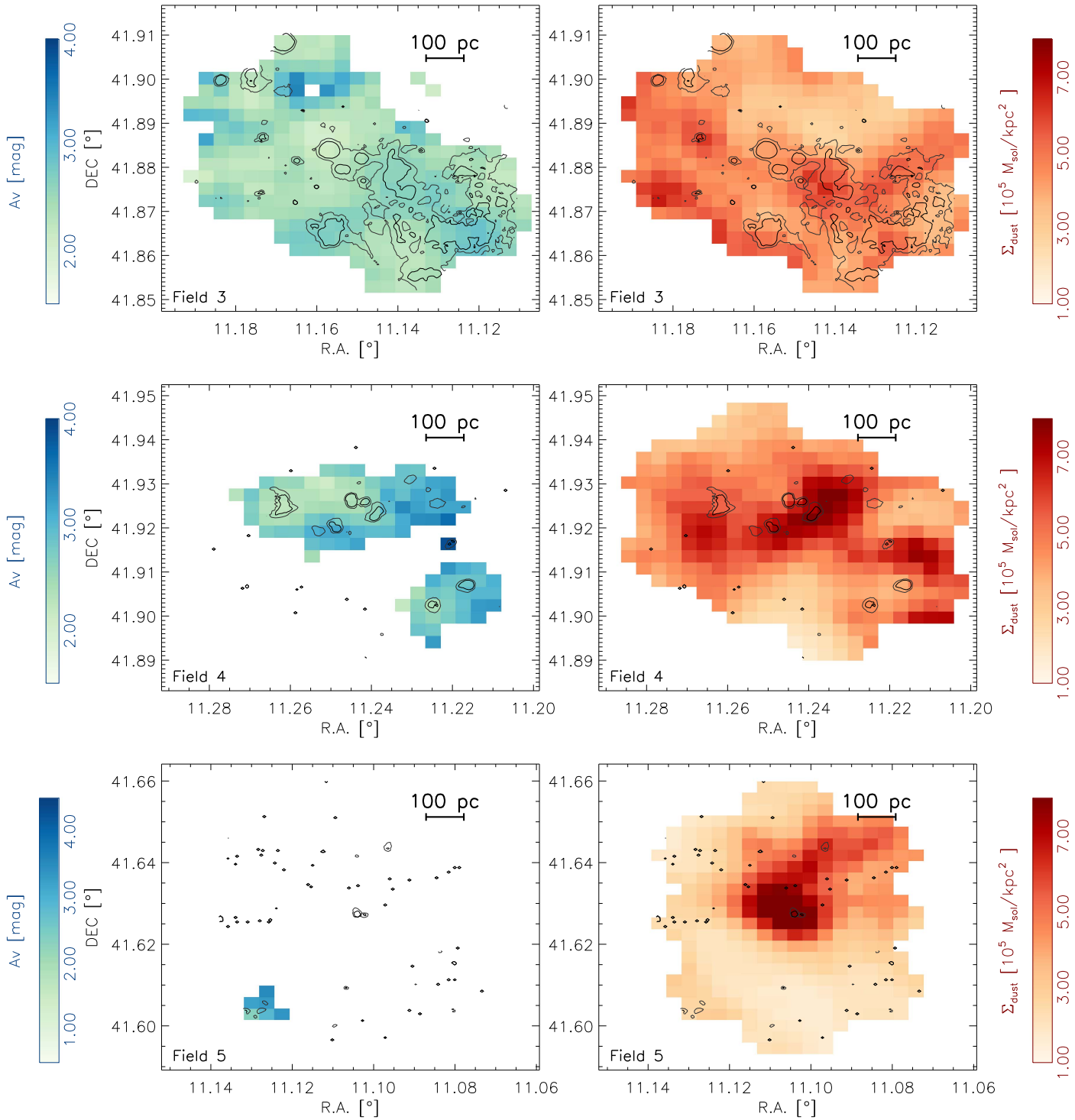

Figure 5. Attenuation (A_V, left) and dust mass surface density maps (Σ_{dust}, right) for Fields 3 (top), 4 (middle), and 5 (bottom). Contours and scale are as in Figure 4. The attenuation spans a larger range of values compared to Field 1. In general, H II regions are situated mostly in or near the regions of higher dust mass surface density. Due to the low flux and hence S/N of the emission lines in Field 5, there are only four pixels in the convolved map with robust detections.

the dust. The two major models that are used for this work are the "foreground screen" model and the "mixed" model (in Calzetti et al. 1994, these are referred to as the "Uniform dust screen" and the "Internal dust" models). The remaining models are variations on those two extremes.

The "foreground screen" model describes a situation where all the dust sits in a smooth, uniform screen between the emitter and the observer (the dust is not mixed with the sources of radiation). Assuming the dust model from Draine & Li (2007) and the dust-to-gas ratio (DGR) from Draine et al. (2014), the attenuation is linearly related to Σ_{dust} via

$$A_V^{screen} = 0.74 \cdot \frac{\Sigma_{dust}}{10^5 M_\odot \text{ kpc}^{-2}} \text{ (mag)}. \quad (3)$$

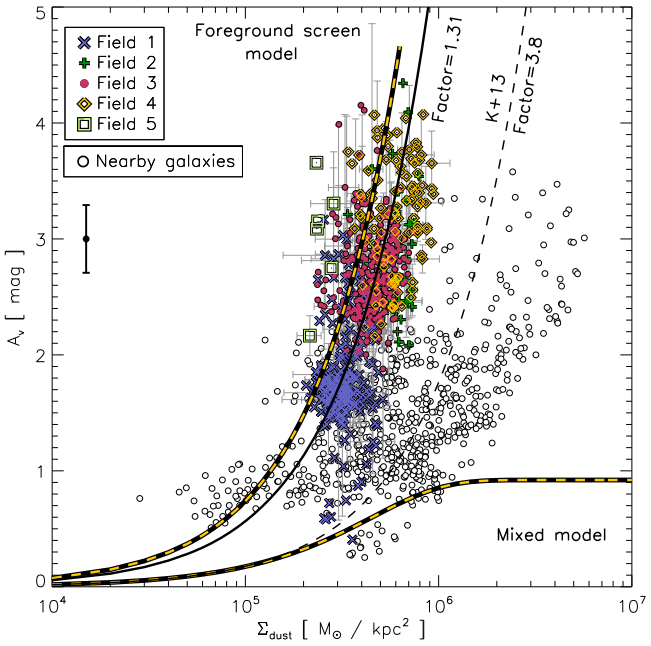

Figure 6. Attenuation (derived from the Hα/Hβ ratio) compared to the dust mass surface density. Foreground screen and mixed models (Calzetti et al. 1994) are represented by thick, black/yellow lines. Various symbols represent data points from our five fields in M31. Data from K13 for nearby galaxies are shown in the background as empty circles. A foreground screen model decreased by a factor of 3.8 (from K13) and 1.35 (best fit for M31) are also shown. The median value of the M31 uncertainties of attenuation values are shown on the left side of the diagram.

Given our assumptions, this equation provides a theoretical upper limit on the attenuation possible at a given dust mass surface density.

The "mixed" model assumes that the dust is uniformly distributed with the sources of radiation. Therefore, the attenuation in the mixed model is much lower than in the foreground screen model. The resulting mixed model attenuation, assuming isotropic scattering and the same connection with dust mass as in Equation (3), is (based on Calzetti et al. 1994)

$$A_{\rm V}^{\rm mixed} = -2.5\log_{10}(\gamma_{\rm V})\,({\rm mag}), \quad (4)$$

where

$$\gamma_{\rm V} = \frac{1 - e^{0.57A_{\rm V}^{\rm screen}}}{0.57A_{\rm V}^{\rm screen}}. \quad (5)$$

γ functionally limits the value of the optical depth in the optically thick medium (Calzetti et al. 1994). The screen model correlates linearly with the dust column, while the mixed model saturates and for high dust mass surface densities yields a moderate expected attenuation (Figure 6).

Figure 6 shows a comparison of the dust mass surface densities and the attenuation for M31 and for the nearby galaxies observed by K13, together with the two Calzetti models. While the data from K13 span the area between the foreground screen and mixed models, the more resolved M31 data follows a foreground screen model more closely. No clear trends are seen within each Field of M31, but when the fields are considered together the data fits the foreground screen model very well. We find the correlation between $A_{\rm V}$ and $\Sigma_{\rm dust}$ to be well fit by scaling down the foreground screen model by a factor of 3.8 for the nearby galaxies (K13) and 1.35 for M31.

We see some regions in M31 that have larger attenuation than is expected from our foreground screen model (Equation (3)). Approximately 25% of the data points are above the foreground screen model, or 3% of the data if we take into account their corresponding 1σ errors. These high A_V regions can be explained by (1) "clumpiness" in the dust below our resolution that is affecting our measured $\Sigma_{\rm dust}$, (2) an underestimation of the dust mass surface density, (3) poor calibration of the optical spectra, (4) values of $A_{\rm V}/\Sigma_{\rm dust}$ different from what we have assumed, and (5) variation in the extinction curve k(λ) that affect $R_{\rm V}$ and thus $A_{\rm V}$.

If an area with low $\Sigma_{\rm dust}$ has locally a high density clump of dust covering the H II region, averaging the dust surface density due to the low spatial resolution of our observations could misleadingly show a low $\Sigma_{\rm dust}$ and a high $A_{\rm V}$. However, when comparing the value of $A_{\rm V}$ around H II regions at PPaK 2.″7 resolution ($\sim$10 pc), we find that $A_{\rm V}$ does not change rapidly with different aperture sizes.

Previous work has tested the accuracy of estimating dust masses using the Draine & Li (2007) model (Alton et al. 2004; Dasyra et al. 2005; Aniano et al. 2012; Galametz et al. 2012; Dalcanton et al. 2015; Planck Collaboration et al. 2016). Most recently, Dalcanton et al. (2015) and Planck Collaboration et al. (2016) measured dust column density within the Milky Way and M31 by measuring the extinction of the light from background sources. Both studies concluded that the Draine & Li (2007) dust model may overestimate the mass of the dust by a factor of $\sim$2.5. Comparisons with independent FIR observations have shown that this offset is not due to uncertainties in the *Herschel* photometry (Verstappen et al. 2013; Planck Collaboration et al. 2016).

Planck Collaboration et al. (2016) suggest that this offset is dependent upon the heating radiation field intensity. In the Appendix, we explore the effects of renormalizing $\Sigma_{\rm dust}$ in M31 and the K13 (Appendix A; Figure 12). Based on this, we would expect that such a normalization would only further the disagreement between the K13 galaxies and M31. However, because this renormalization is not well calibrated in the high interstellar radiation field regime (corresponding to most of the K13 regions), we do not include the renormalization in the following analysis and figures.

An additional effect that can play a role in our derived attenuation is the "mid-plane" effect, because we expect half of the dust to be situated behind the ionizing sources. That can partly explain the offset of M31 data from the "foreground screen" model line. This effect should be strongest in the case where the scale height of the ionized gas is much smaller than the scale height of the dust. However, in the case of similar scale heights, this effect should play a much smaller role.

Given our confidence in our spectrophotometric calibration, we explain higher attenuation values of some regions as a result of possible variations in the extinction law tied to variations in the dust properties, which we expect to be related to variations in our assumed DGR and $R_{\rm V}$.

4. Discussion

Our main result (Figure 6) shows that M31 more closely follows a foreground screen model than a mixed model. This is different from what K13 found in nearby galaxies. In this section, we consider various factors that potentially explain the

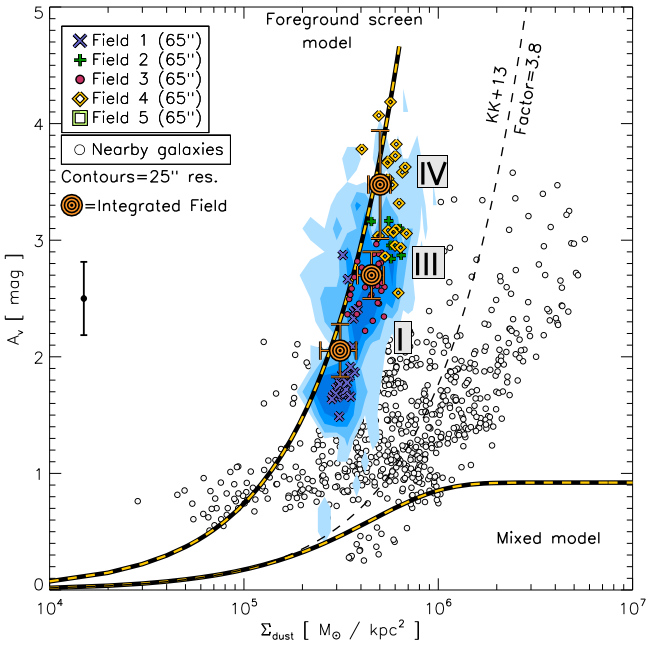

Figure 7. A_V vs. Σ_{dust} for our M31 fields convolved to different spatial scales. Contours show the data from Figure 6 at 24.″9 scales(∼100 pc), the various symbols represent the data at 65″ scales (≈260 pc), while the big circles indicate results from integrating each Field (as labeled) spanning spatial scales of 0.6 kpc × 0.9 kpc. Due to the low AoN of Hβ, only three fields can be shown. No obvious change in the A_V vs. Σ_{dust} relation is apparent between the different resolutions. 1σ uncertainty error bars for the integrated fields and the median uncertainty of the convolved data (shown in the left corner) are presented. Systematic uncertainties in the spectral fitting dominate over the random instrumental uncertainties.

differences between these results. We examine the effect of physical resolution on attenuation (Section 4.1). We test the effects of a spatially extended ionized gas component on attenuation (Section 4.2). We associate this additional gas with diffuse ionized gas (DIG) and discuss the effects of different scale heights of dust, H II regions and DIG on A_V (Sections 4.2, 4.3 and 4.4). Finally, we explain the varying vertical distribution of dust and gas in M31 and the K13 galaxies by observations at different galactic radii (Section 4.5).

4.1. The Impact of Physical Resolution

While K13 probed spatial scales between ∼0.3 and ∼2 kpc, the proximity of M31 means that the SPIRE 350 μm physical resolution is ∼100 pc. The fields in M31 are located within the most dense and dusty spiral arms and cover only a small fraction of the galaxy. Therefore, it is possible that our M31 results are biased by dusty, star-forming regions, where a foreground screen model more closely represents the dust distribution. The larger physical sizes of the regions sampled in K13 can probe both regions where a foreground screen model is more representative and regions where a mixed model more closely matches reality. This yields a result where together all regions show a mixture between the two models. K13 searched for a correlation between A_V–Σ_{dust} slope and different spatial scales, but the changes in slope were not significant.

To directly compare our result with K13 (whose best spatial resolution is ≈300 pc), we smoothed our data (Figure 7) to 65″ resolution (corresponding to spatial scales of ≈260 pc) and find no difference in the slope of the correlation. Moreover, we also integrate all spectra from each field into a single data point and re-extract the line fluxes to determine the average attenuation for each field. Resulting integrated field data points span spatial scales of around 0.6 kpc × 0.9 kpc. We then compare this value to the average dust mass surface density for the field. Integrated field data points are shown as circles in Figure 7, and it is clear that even at these scales we see the same relation between attenuation and dust mass surface density. Some fields are not presented, due to the low number and brightness of H II regions. Because the Hβ line is faint, this results in low AoN values for those fields.

The regions in K13 target wide areas (covering both spiral arms and inter-arm regions) and can consist of regions with or without low-brightness H II regions. It is possible that the dust probed in some of those regions is heated by an old stellar population and not solely by H II regions. However, because the Draine & Li (2007) model explicitly takes into account starlight heating, the modeled dust mass should not suffer from any bias in either K13 or our results on any of the scales considered. Using the close alignment of disk galaxies in front of early-types, Holwerda & Keel (2013) found that inter-arm regions contain less dust relative to spiral arms. While K13 included regions with a broad range of dust mass surface densities, the regions with weak Hα flux (where dust may be predominantly heated by the old stellar population) are generally removed by the S/N criteria in their work. Therefore, we conclude that the difference between our results and theirs is not related to the treatment of the inter-arm regions. However, the integrated fields of M31, which have a similar spatial resolution to K13 ones, have SFR surface densities (Σ_{SFR}) that are a factor of 10 lower. This makes a direct comparison between fields at fixed Σ_{SFR} impossible. The mean Σ_{SFR} in M31 is around $\sim 0.01\,M_\odot\,yr^{-1}\,kpc^{-2}$, while for the K13 galaxies Σ_{SFR} spans a 0.03–10 $M_\odot\,yr^{-1}\,kpc^{-2}$ range (Appendix B; Figure 13).

4.2. Effects of an Additional Component to the Dust/Gas Distribution Model

Another possibility to explain the difference in the A_V–Σ_{dust} relation between M31 and the K13 galaxies is that, in the K13 galaxies, some fraction of the ionized gas resides outside the dust disk. This emission would not be extinguished, therefore, lowering the observed A_V. In this section, we propose the DIG as a candidate for this gas outside the dust disk. We also explain why the previously used Calzetti et al. (1994) model of dust/gas distribution (combining only H II regions, stars and dust) requires an additional diffuse and spatially extended component.

4.2.1. Additional Flux from Non-attenuated Gas

The Calzetti et al. (1994) model for the dust/gas distribution combines only dust and stars (that ionize the gas within the H II regions). That model neglects the possibility of additional flux from ionized gas spatially even more extended than the dust. In the scenario where additional gas resides outside the dust disk, the observed attenuation would be lower than in the case of the Calzetti et al. (1994) model, even for the same observed amount of dust. If we assume that the M31 regions have all of the ionized gas embedded in the dust disk, we explore how flux

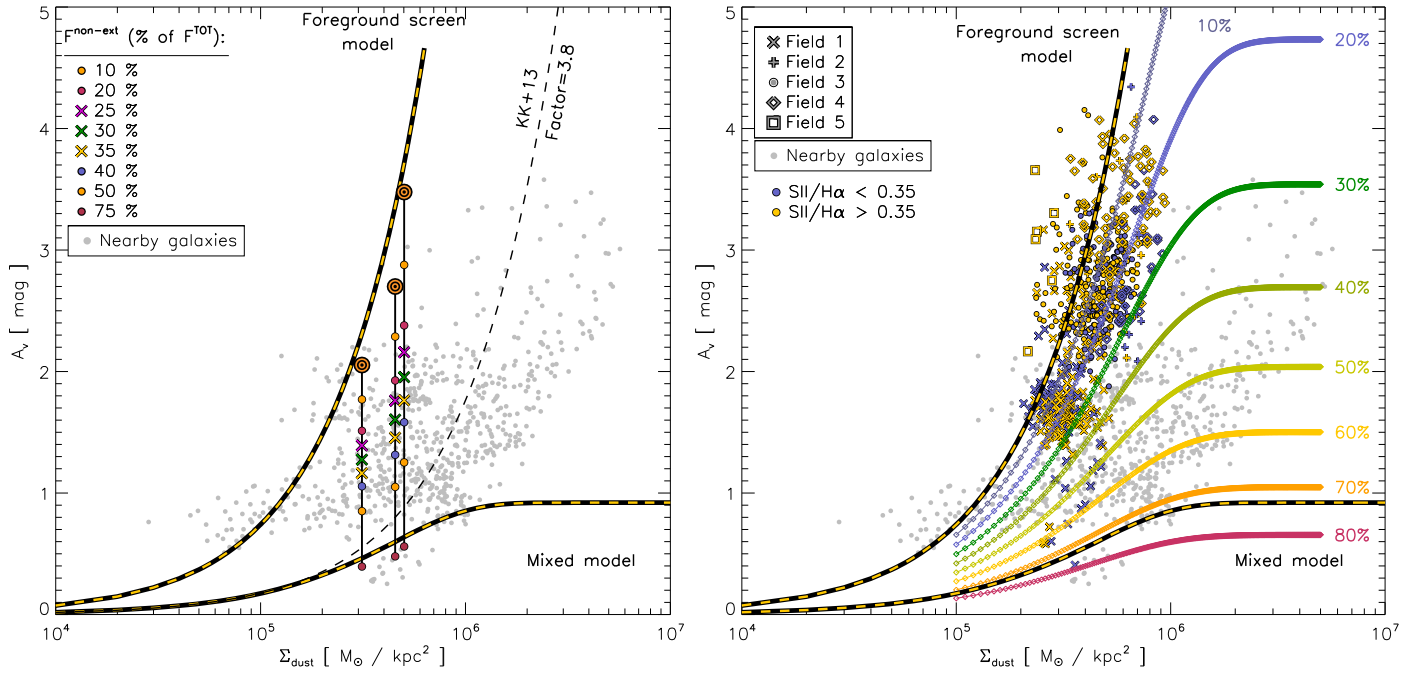

Figure 8. Impact on attenuation when flux from non-attenuated ionized gas ($F^{\rm non\text{-}ext}$) is added outside the dust disk. $F^{\rm non\text{-}ext}$ is shown as a percentage of the total observed flux $F^{\rm tot}$. The left panel shows the impact on A_V for integrated fields in M31 when we add non-attenuated flux. The right panel shows the impact of unattenuated emission on the foreground screen model. The lines on the right panel better reproduce the trend and slope of the K13 data than the scaling factor of 3.8 for the foreground screen model proposed by K13. Some lines are situated below the mixed model limit predicted by Calzetti et al. (1994) because the Calzetti model does not include a contribution from spatially extended, non-attenuated ionized gas. The M31 data in the right panel are color-coded according to their [S II]/Hα ratio (yellow for DIG and blue for H II region dominated).

from a non-attenuated ionized gas, which may lie outside the dust disk, would effect the A_V–$\Sigma_{\rm dust}$ relation.

In Figure 8, we investigate how large the contribution from a non-attenuated ionized gas component above the dust disk would need to be in order for the M31 data to follow the trend of K13. Hα flux from that non-attenuated ionized gas, $F^{\rm non\text{-}ext}$, is presented as a percentage of the total observed flux, $F^{\rm tot}$. For M31, we assume that no ionized gas is outside the dust disk. The left panel in Figure 8 shows the impact on our integrated fields in M31 when we add flux from such an additional ionized gas outside the dust disk. Similarly, the right panel shows the impact of that additional ionized gas on the foreground screen model. Even a small amount of flux from the added ionized gas lowers the attenuation enough that we observe values similar to those found by K13.

If 30%–60% of the observed total Hα flux arises from gas that sits outside the dust disk, we can recover the relation observed by K13 within nearby galaxies. This provides a better qualitative fit than simply scaling the foreground screen model by a factor of 3.8, as suggested by K13 (Figure 8, right panel). When the contribution from the additional ionized gas component to the emission is large, our model drops even below the "mixed" model curve. This is because, unlike the Calzetti model, we are including a component with no attenuation at all in the model. At extreme contributions, we would only see the non-attenuated component and measure little to no total attenuation.

It is not expected that the ionzied gas directly associated with H II regions will span large spatial scales because typical H II region sizes are less than 100 pc (Azimlu et al. 2011). However, a good candidate for the extended ionized gas component we propose here is the DIG.

4.2.2. DIG as an Additional Component

DIG (also known as the Warm Ionized Medium or WIM; Reynolds 1971; Walterbos & Braun 1994; Greenawalt et al. 1998; Wang et al. 1999; Oey et al. 2007; Haffner et al. 2009) extends within and outside the galactic disk. Unlike H II regions and most of the dust, which reside within a thin disk and span scale heights of only $\approx$100 pc, the DIG can extend above and below the disk out to kiloparsec scales, similar to the thick disk component (Reynolds 1984; Haffner et al. 2009; Bocchio et al. 2016). Previous studies have shown that the scale height, location, and brightness of the DIG follows the brightness and location of star-forming regions (Dettmar 1990; Dettmar & Schultz 1992; Ferguson et al. 1996, 1998; Rand 1998; Wang et al. 1999; Collins et al. 2000; Rand 2005; Heald et al. 2006; Oey et al. 2007). The DIG can be a good candidate for the extended ionized gas, which may lie outside the dust disk and may affect the attenuation. Due to the approximately kiloparsec physical resolution observed by K13, they were unable to distinguish the emission arising from H II regions and the DIG.

Physically, the DIG is warmer and less dense than gas in H II regions. In the DIG regions, the [S II](λ6717 + λ6731)/Hα ratio is higher (>0.4, while for the H II regions it is usually <0.2; Minter & Balser 1998; Haffner et al. 2009). The origin of ionization in the DIG is speculative, but is likely due to a combination of supernova shocks, turbulent dissipation, leaked radiation from nearby OB stars, additional photons provided along channels in the neutral gas, and heating by cosmic rays or dust grains (Reynolds 1990; Reynolds & Cox 1992; Minter & Balser 1998; Madsen et al. 2006; Haffner et al. 2009; Barnes et al. 2014, 2015; Ascasibar et al. 2016).

In M31, Walterbos & Braun (1994) found that after masking all H II regions the DIG flux contributes, on average, around

40% of the total Hα flux (or 20% after extinction corrections). This percentage varies between the observed fields in M31 (Walterbos & Braun 1994) and is observed to vary greatly between galaxies (Haffner et al. 2009).

The DIG fraction we detect in our fields in M31 agrees with the results of Walterbos & Braun (1994); after masking H II regions using an intensity threshold of 2×10^{-16} erg s^{-1} cm^{-2} arcsec^{-2} (as used in Walterbos & Braun 1994), the contribution of DIG flux to the total flux of the fields varies between 40% (Fields 1 and 3) and 70% (Fields 2 and 4). Most of the emission in Field 5 is composed of DIG flux (based on this threshold value). The line ratio of [S II]/Hα is ≈0.5 throughout our fields and the fields observed in Walterbos & Braun (1994; which are almost five times larger).

The intrinsic Hα/Hβ ratio of the DIG is likely to be higher given the higher temperature, but we assume it to be 2.86 for simplicity. Using ITERA[13] (Groves & Allen 2010), we conclude that the intrinsic Balmer line ratio of DIG can have values between 2.75 and 3.1, depending on the exact temperature, ionization parameter, magnetic field strength, and density. Even if the intrinsic ratio is an extreme value of 3.1, the attenuation values would be lower by only approximately 0.3–0.5 mag from those currently shown in Figure 6, which would not dramatically change our results. Therefore, in the following, we assume the same intrinsic ratio while calculating the A_V of the DIG.

4.2.3. Effects of Different Dust-H II-DIG Distributions on A_V

The relative distribution and differences in scale heights between H II, DIG, and dust can change our derived attenuation even if the relative amounts stay the same. For example, if both components of ionized gas (DIG and H II regions) have smaller scale heights compared to the dust, the derived A_V of both components would only correlate with Σ_{dust}. If the DIG resides outside the dust (i.e., has a larger scale height), the average A_V of the ionized gas (combining both H II region and DIG emission) will be lower for the same Σ_{dust}. That scenario is equivalent to the one tested in Figure 8 (Section 4.2.1).

Multiple results indicate the need for more complex dust distribution models within galaxies in order to match simulations and observations (Wong & Blitz 2002; Popescu et al. 2011; Viaene et al. 2017). Wong & Blitz (2002) proposed a "hybrid" model where dust behaves differently in the region located in the center/inner and outer disk of galaxies. In the central regions of galaxies, where molecular gas dominates, the dust is more dense and has a smaller scale height. In the outer regions of galaxies, where the H I gas dominates, the dust is more diffuse and vertically more extended. This complexity in the dust scale height may explain the difference between M31 and the galaxies studied by K13.

If we assume that in M31 the ionized gas (H II and DIG regions) resides within the dust layer (partly mixed with the dust and partly obscured by a dust screen), then the attenuation would follow the slope of the foreground screen model. For the nearby galaxies in K13, we propose that the DIG resides outside the dust and that dust and gas are not mixed. In that case, the non-attenuated flux from the DIG contributes to the already attenuated flux from H II regions (which lie within the dust), and lowers the overall attenuation. It is unlikely that there is no attenuation at all of the DIG component because it is probably mixed with the diffuse dust component in the thick disk (Howk 2012; Bocchio et al. 2016). However, for simplicity, we assume that most of the DIG in nearby galaxies does not mix and is external to the dust.

In conclusion, unlike the previously used Calzetti models of dust/gas distribution (combining H II regions, stars, and dust), our results indicate that by adding a weakly or unattenuated DIG component to those models, the attenuation can change significantly. The contribution of a DIG component also yields higher [S II]/Hα ratios than in H II regions, which cannot be explained by the Calzetti models alone (see Section 4.3). Therefore, the contribution of the DIG component and its relative vertical distribution (i.e., scale height) compared to the dust disk can explain the discrepancy between the nearby galaxies analyzed by K13 and our result in M31.

4.3. [S II](λ6717 + λ6731)/Hα versus A_V Diagram

In the case where the DIG resides outside the dust disk and does affect our observations, we expect areas with higher [S II]/Hα and the same Σ_{dust} to have a lower A_V. There would be no trend between A_V and [S II]/Hα (at the same Σ_{dust}) if both components lie within the dust disk.

In Figure 8, our M31 data are color-coded according to their [S II]/Hα ratio (with 0.35 as a threshold). Data points with lower ratios indicate areas with H II regions, while those with higher ratios mark DIG-dominated areas. Our M31 fields do not show a clear trend between the [S II]/Hα ratio and A_V, with Field 4 even exhibiting lower line ratios for regions lying further away from the foreground screen model. Due to possible changes of the intrinsic Balmer line ratio in DIG-dominated spaxels, A_V values of those spaxels could drop down to 0.3–0.5 mag from those currently shown in Figure 8. K13 showed that there is a trend for a higher [S II]/Hα ratio at lower attenuation in all their galaxies, which they attribute to the fact that H II regions are located within dusty birth clouds (Figure 4 in K13). Because the two lines are very close in wavelength, extinction alone cannot account for the change in the [S II]/ Hα line ratio (at $A_V = 3$ mag the change is only 0.02 in the ratio).

Figure 9 shows [S II]/Hα as a function of A_V for regions within nearby galaxies (left panel) and M31 (right panel), color-coded by the dust column density. In both panels, the contours indicate the distribution of the data for nearby galaxies at 2.″7 resolution. In the left panel of Figure 9, the regions within nearby galaxies are convolved to 18″ resolution (spanning physical scales between ≈300 and ≈2000 pc). NGC 2146 (*X* symbols) is an outlier in this diagram as it has a high inclination, high dust column galaxy, with clear shock driven outflows (Kreckel et al. 2014). In the right panel of Figure 9, our M31 data are shown at 24.″9 resolution (≈100 pc) and the integrated fields.

In general, the change in spatial scales affects our line ratios by diluting the flux from compact, resolved objects like H II regions. H II regions within M31 (with [S II]/Hα < 0.3 at 10 pc scales) exhibit higher [S II]/Hα ratios when convolved to 100 pc scales. The same diluting effect causes a decrease in the [S II]/Hα ratio for regions dominated by extended DIG emission.

Some areas (20% of all regions and almost half of Fields 2, 4, and 5) are consistent with shock excitation ([S II]/Hα > 0.5, Kewley et al. 2006); however, they also show large

[13] IDL Tool for Emission-line Ratio Analysis.

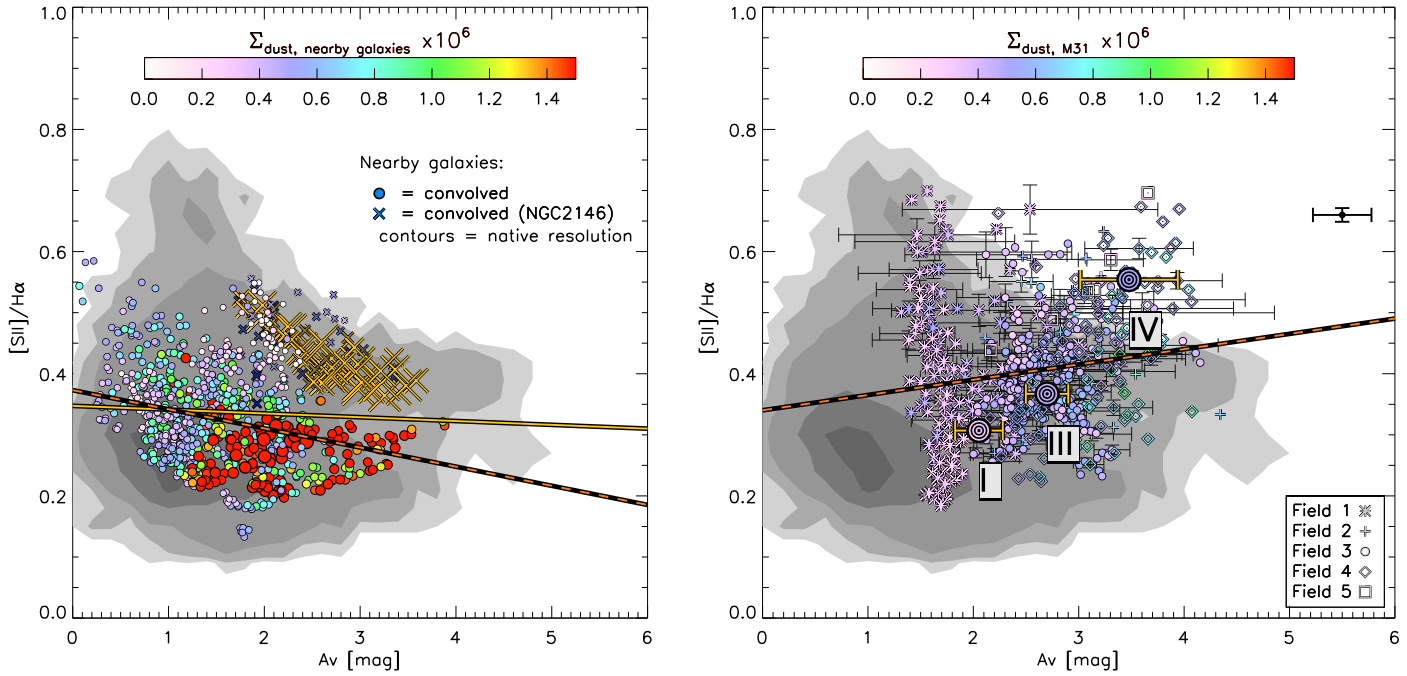

Figure 9. [S II](λ6716+λ6730)/Hα vs. A_V diagrams of nearby galaxies (left) and M31 (right). Contours in both diagrams represent the K13 data points at native PPaK (24.″9) resolution. Left: convolved (18″ resolution) data points for the K13 nearby galaxies, colored and in sizes according to Σ_{dust}. The yellow line shows the trend of convolved data of all galaxies while the orange dashed line shows the trend of the sample without NGC 2146. Right: convolved (24.″9 resolution) and integrated field data points for M31, also colored by Σ_{dust} values. The orange dashed line shows the trends of the convolved data. Error bars are shown for a representative sample of the data, and the median value of all uncertainties (right corner) is also shown.

uncertainties (due to low S/Ns, as they have low surface brightness).

The left panel in Figure 9 does not show a clear trend for lower attenuation at higher [S II]/Hα ratios. However, some of the individual galaxies in the K13 sample (like NGC 3627, NGC 6946, and NGC 3077) do show a weak trend for increased [S II]/Hα toward lower A_V. Shown in the right panel of Figure 9, the M31 data actually suggests an increase of the [S II]/Hα ratio with A_V. However, there is a large scatter, and this trend is predominantly driven by variation between the fields, suggesting some dependence on location and physical characteristics of ISM (see Section 4.4).

We could miss certain spaxels with both higher [S II]/Hα ratio and A_V due to the faintness of the lines (caused by both low surface brightness and high attenuation). Such spaxels could possibly change the trends seen in Figure 9.

There is a possibility that the gas-phase metallicity has an effect on the global trend in line ratios. Like most galaxies, there exists a radial metallicity gradient in M31 meaning the metallicity increases from Fields 1 to 5 (Table 3 in Kapala et al. 2015; Zurita & Bresolin 2012; Draine et al. 2014). This higher metallicity is associated with the higher DGR and the higher [S II]/Ha ratio. However, this ratio is affected not only by metallicity, but also by ionization parameter and temperature of the gas, and this degeneracy causes issues in the analysis of the ratio and A_V.

Besides the difference in trends, thresholds, and biases on A_V, M31 shows higher attenuation at fixed dust mass surface density, and a higher [S II]/Hα ratio at fixed A_V (especially at higher A_V) compared to other nearby galaxies (as seen in Figures 6 and 9). More complicated models are required to better understand the affects of the different relative scale heights of dust, H II regions, and DIG on the line ratios and on A_V.

4.4. Modeling the Impact of Geometry

In this sub-section, we investigate two simple models that examine how the vertical distribution (scale heights) and intensity of the H II and DIG phases compared to the dust layer can change the observed values and relations between Σ_{dust}, A_V, and the [S II]/Hα ratio.

The first simple model (Figure 10) represents a face-on galactic disk composed of only a thin layer of H II regions (with [S II]/Hα = 0.15), a uniform dust screen, and a DIG component in front (with [S II]/Hα = 0.75), all along one line of sight. We took those specific S II/Hα ratios for simplicity, but in a real ISM those values could change. In this model, one resolution element includes emission from an H II region, that suffers an attenuation A_V^{real} from the dust screen. The emission from the DIG is assumed to be unattenuated. The variables that are changed in the model are (1) the intrinsic attenuation A_V^{real} (directly proportional to Σ_{dust}) and (2) the ratio of intrinsic intensities from the DIG and the H II region (parameter $X = I^{DIG}/I^{H\,II}$). We emphasize that $I^{H\,II}$ is not attenuated and cannot be associated with the value F^{ext} described in the previous section. By varying these parameters, we can then explore the changes in the observed [S II]/Hα ratio (hereafter labeled S2) and A_V^{obs}. This toy model is insensitive to spatial scales and to the amount of flux because all variables are relative to each other.

In the left panel of Figure 10, we show the correlation between S2, the intrinsic and observed attenuation, and the ratio of intrinsic intensities from the DIG compared to H II regions (parameter X). Our model indicates that different combinations of emission from DIG and H II regions can generate the same observed S2 and A_V values for a range of dust masses (i.e., $\sim A_V^{real}$). This is because of the large impact the DIG emission has on the S2 and A_V values when the flux

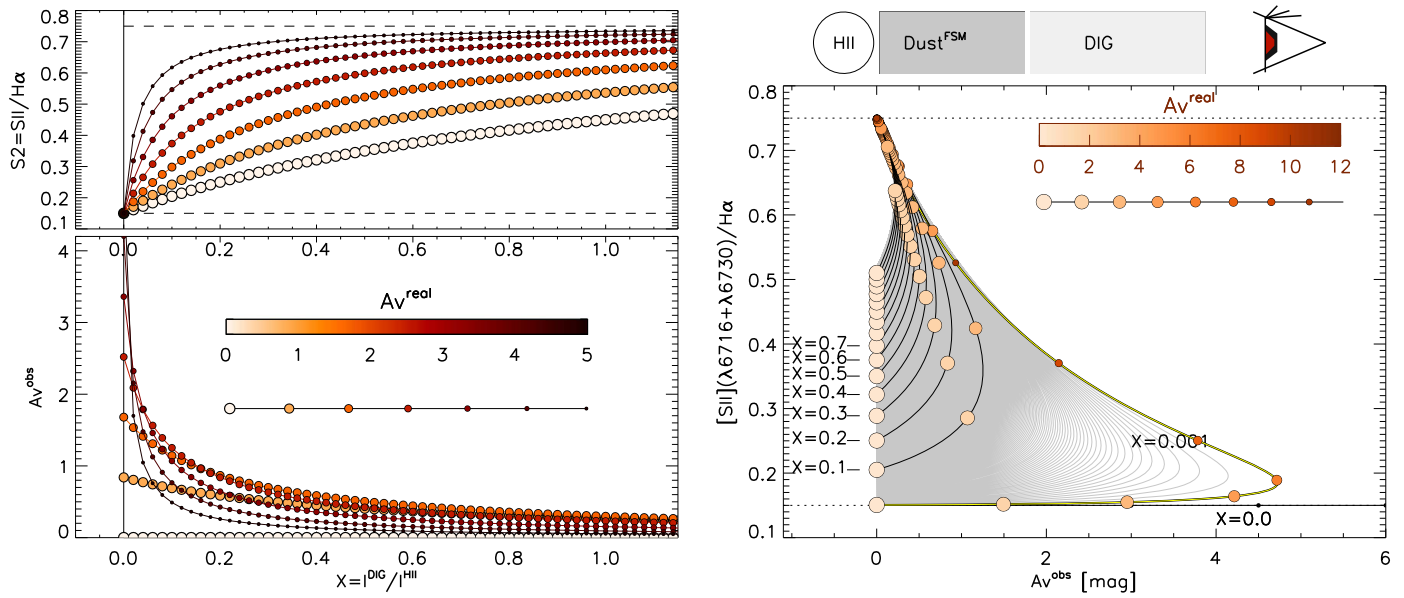

Figure 10. Simplified model (diagram presented above the right panel) that explores the relationship between the observed line ratios and the spatial geometry of dust, H II, and DIG regions in the LOS of a face-on disk. In this model, between the observer and the H II region (with an intrinsic brightness $I^{\rm H\,II}$ and S2 = [S II]/Hα ratio of 0.15) is a layer of dust screen (labeled as Dust$^{\rm FSC}$ and proportional to $A_{\rm V}^{\rm real}$) and DIG (with an intrinsic brightness $I^{\rm DIG} = X \cdot I^{\rm H\,II}$ and S2 = 0.75). Left: as an input to the model, we have the amount of dust ($A_{\rm V}^{\rm real}$), upper and lower limits of S2 (0.15 and 0.75), and ratio between H II and DIG intensity (or X). The correlation between those parameters (upper left panel) and the resulting observed attenuation $A_{\rm V}^{\rm obs}$ can be seen in the lower left panel. Notice that the observed attenuation does not follow the real attenuation and that there are overlaps where one value of $A_{\rm V}^{\rm obs}$ can have multiple values of $\Sigma_{\rm dust}$ (depending on X). Right: the correlation between the observed S2 = [S II]/Hα ratio and the observed attenuation $A_{\rm V}^{\rm obs}$ with different ratios of DIG and H II intensities (shown as X) and different values of $\Sigma_{\rm dust}$ (shown through $A_{\rm V}^{\rm real}$). Notice the resemblance between this image and those in the left panel of Figure 9. See the text for more details.

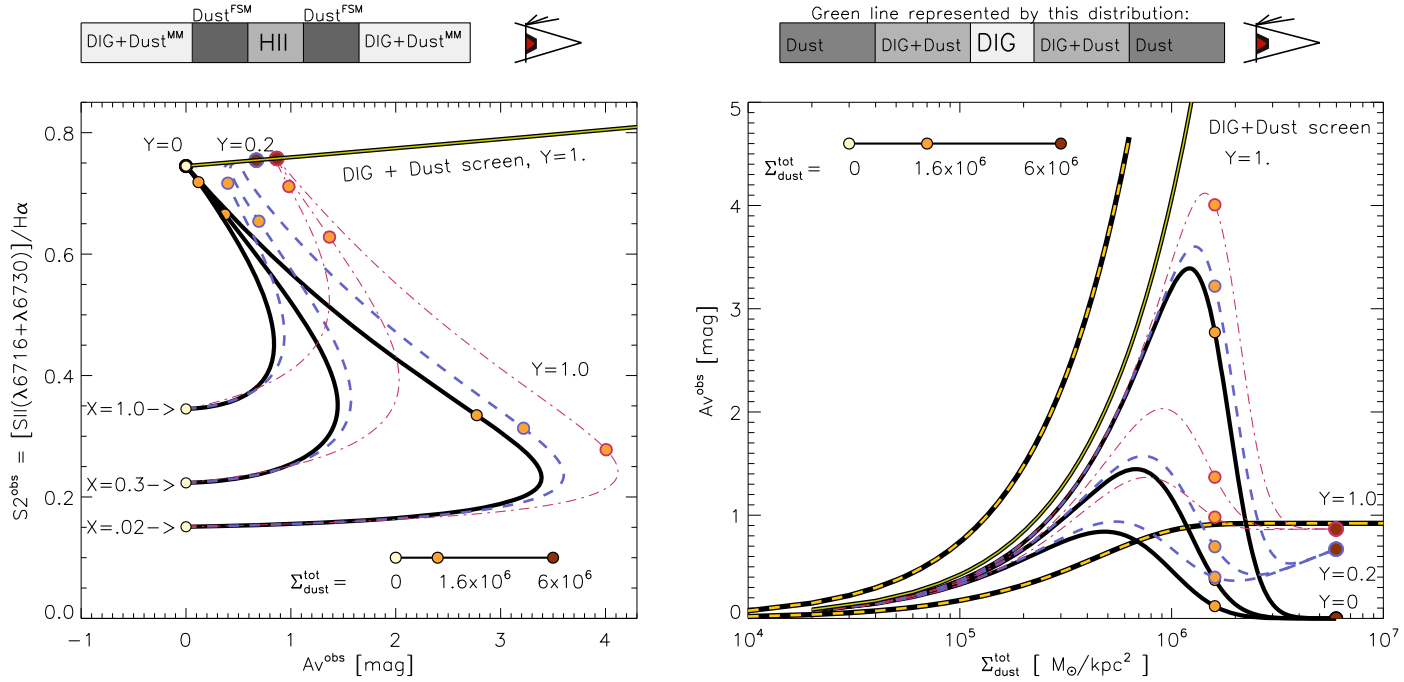

Figure 11. Second model (left panel on top), similar to the previous model (Figure 9), but with a more realistic ISM distribution: DIG (mixed with the diffuse dust layer) and the dust screens lie on both sides of the H II region. The left panel shows [S II]/Hα vs. $A_{\rm V}^{\rm obs}$, while the right panel shows $A_{\rm V}^{\rm obs}$ vs. $\Sigma_{\rm dust}^{\rm tot}$. The diagrams show the relationship between the observed attenuation ($A_{\rm V}^{\rm obs}$), the [S II]/Hα ratio (S2) with the model variables: the observed total dust column density ($\Sigma_{\rm dust}^{\rm tot}$), the relative intensities of the DIG and H II regions ($X = I^{\rm DIG}/I^{\rm H\,II}$), and the ratio of the dust mixed with DIG to the total dust column ($Y = \Sigma_{\rm dust}^{\rm DIG}/\Sigma_{\rm dust}^{\rm tot}$). We assumed the same specific intrinsic S2 values for the gas in H II and DIG as in Figure 10. Values of $Y = 0$, 0.2, and 1.0 are shown in black (full), blue (dashed), and red (dotted–dashed) lines. We also include the green, full line that represents a scenario (shown above the right panel), where 90% of DIG is mixed with dust (while 10% lie in the center and is not mixed with dust). This scenario also assumes length of the dust layer twice as large as the length of the ionized gas layer, thus representing our assumption about dust/gas distribution of M31. With this scenario, we can reproduce the regions with higher $A_{\rm V}^{\rm obs}$ and S II/Hα ratios seen in Figure 9.

from the H II region is highly attenuated. Combining that effect with the dependence of S2 on the dust and the DIG, our model resembles the behavior observed for nearby galaxies (Figure 9). However, this model cannot explain the data for M31, where we observe high values of [S II]/Hα and A_V, nor explain the offset in attenuation between regions at fixed dust mass surface density in M31 and the other nearby galaxies.

The second model (Figure 11) has a more realistic ISM distribution where the layers of DIG and diffuse dust lie on both sides of the H II region and are mixed, as observed by Howk (2012). The left panel shows [S II]/Hα versus A_V^{obs}, while the right panel shows A_V^{obs} versus Σ_{dust}^{tot}. In this model, we assume that a certain amount of diffuse dust is mixed with the DIG. The mass of mixed dust is given by the ratio of mixed to total dust mass (parameter $Y = \Sigma_{dust}^{DIG}/\Sigma_{dust}^{tot}$). Σ_{dust}^{tot} is equivalent to the total observed dust and it is a sum of the dust layer around the H II region, which acts as a screen (labeled as $Dust^{FSC}$ in Figure 11) and the dust layer mixed with DIG (labeled as $Dust^{MM}$ in Figure 11).

In the second model, shown in Figure 11, a case of $Y = 0$ represents the case where the dust is not mixed with DIG and there is no $Dust^{MM}$. That is the case similar to the first model shown in Figure 10. When we redistribute the total dust so that some part of it is mixed with the DIG (thus rising value Y), the dust dims the DIG emission and increases the measured attenuation. We present an extra scenario in Figure 11, where there is only DIG and dust and the scale height of the DIG is smaller than the scale height of the dust layer. That scenario shows higher A_V^{obs} and higher S II/Hα ratios compared to previous cases. With that scenario, we can reproduce the regions with higher attenuation and higher [S II]/Hα ratio noticed in Figures 8 and 9.

Comparing the K13 and M31 data seen in Figures 6 and 9 with the models in Figures 10 and 11, we notice complex behaviors and the strong effect the DIG vertical distribution has on the observed A_V^{obs} and S II/Hα ratios.

In the nearby galaxies studied by K13, the DIG components could be more extended and not so well mixed with the dust. We draw this conclusion by comparing the observed ratios in Figure 9 with the simple models on Figures 10 and 11. The likely difference between those galaxies and M31 is the intensity and relative vertical distribution of dust and DIG.

Unlike K13, the higher spatial resolution data in M31 enables us to clearly distinguish between compact H II regions and those regions with dust and DIG only. Our results indicate that the DIG component in M31 could be smaller in intensity and scale height, and be well mixed with the dust layers in the disk. An additional layer of diffuse dust, extending to even larger scale heights than the DIG, would increase the attenuation even more.

The high inclination of M31 likely plays an additional role in increasing the attenuation. Nevertheless, K13 did not report any significant correlation or change in their relation with inclination. For example, the highly inclined galaxy NGC 3627 (similar to M31) shows lower A_V than M31, while NGC 4321 has higher A_V values despite its lower inclination (30°) and similar Σ_{dust} as NGC 3627. NGC 2146 and NGC 7331 are both highly inclined (60° and 70° as M31) but have slightly lower A_V value than those seen in M31.

4.5. Effects of Location on the Relative Vertical Distribution of Dust and DIG

Given these findings, the question that arises is, why in M31 do we observe a different mixture and scale heights between all three components (DIG, H II regions, and the dust) compared to other galaxies? To explain this, we consider the effects of probing different locations within the galactic disk.

We note that the locations and radii of the fields observed in M31 and in K13 are different. In M31, we observe five small fields within the spiral arms of M31, where the most central field is still ~6 kpc from the galaxy center (equal to 0.28 R_{25}; Table 1, de Vaucouleurs et al. 1991; Zurita & Bresolin 2012). The regions observed by K13 are more central ($<0.2\,R_{25}$, except for one galaxy with $<0.4\,R_{25}$), and composed of bulges, spiral arms, and inter-arm regions. The global SFR and Σ_{SFR} for the nearby galaxies studied by K13 are much higher than that of M31 (SFR $\sim 1\,M_\odot\,yr^{-1}$; Williams 2003) and the observed fields ($\Sigma_{SFR} \sim 0.01\,M_\odot\,yr^{-1}\,kpc^{-2}$; see Figure 13 in Appendix B).

If we assume that the dust follows the gas, as seen in Hughes et al. (2014) and Holwerda et al. (2012) with some dependence on dust temperature, then we can argue that the scale height of the dust is equal to the gas scale height and follows it. In several observations, the scale heights of the gas have been found to increase with galactic radius (Sancisi & Allen 1979; Braun 1991; Rupen 1991; Scoville et al. 1993; Olling 1996; García-Burillo et al. 1999; Wong & Blitz 2002; Matthews & Wood 2003; O'Brien et al. 2010; Velusamy & Langer 2014; Yim et al. 2014; Zschaechner & Rand 2015). The increase of the gas scale height can be understood via the gravitational and hydrodynamical equilibrium of the gas, and its dependence on gas vertical velocity dispersion, stellar volume density, and gas surface density (Koyama & Ostriker 2009; Pety et al. 2013). If the dust and molecular gas are correlated, then the dust scale height is rising with galactic radius.

On the other hand, the DIG scale height and intensity are correlated with the number and brightness of H II regions and star-formation activity (Dettmar 1990; Rand 1996; Wang et al. 1999; Collins et al. 2000; Oey et al. 2007). Numerous, brighter star-forming regions that are more energetically active (Tyler et al. 2004; Yasui et al. 2015) can affect the production, destruction, and distribution of dust and also the ionization of the DIG. This can result in a more prominent and extended DIG component. Moreover, Dettmar (1990) noticed a decrease of the Hα scale height with galactic radius (with the highest scale height seen in the starbust regions in the center). We argue that if the scale height of the DIG is proportional to the star-formation intensity, then the decrease of star formation with radius would indicate a decrease of the scale height of the DIG component. Regan et al. (2006) and Bigiel et al. (2010) found the FUV and 8 μm emission (both correlated to star formation) are decreasing with galactic radius and have their highest values in the centers of galaxies. Furthermore, García-Burillo et al. (1999) noticed the existence of Hα chimneys spanning the extra-planar area from the galactic center with scale height larger than that of the CO.

Since the dust scale height is likely to increase with galactic radius while the DIG scale height should decrease with galactic radius, differences in the relative DIG/dust geometry and scale heights of galaxy centers (as in K13 galaxies) and galactic outskirts (as in M31) may explain the differences in our derived attenuation.

5. Wider Implications

In order to determine the spatial distribution of dust compared to the ionized gas, we use the models derived by Caplan & Deharveng (1986). The only components of that model are the dust and ionizing stars and their spatial configuration, which affects the observed attenuation (Caplan & Deharveng 1986; Calzetti et al. 1994). Our results (Figure 6) show that the regions we observe in M31 closely follow a foreground screen model, while K13 showed that most of the regions they selected in a sample of nearby galaxies fall between the mixed and screen models. Furthermore, Liu et al. (2013) in M83 find that the data points of the central region follow more a mixed model, while the outer regions are in agreement with a foreground screen model. Tests show that neither inclination (K13) nor changes in spatial scales (Figure 7) can explain the differences between those results. However, by degrading the spatial resolution of the data (toward $\geqslant$100–200 pc scales) in the central region of M83, Liu et al. (2013) showed that their data begin to follow more closely a foreground screen model. While such results are suggestive, their interpretation should be done with caution, given the large uncertainties, large scatter in the data and the small separation of the models in the diagrams.

Our observation of varying [S II]/Hα line ratios and modeling of the impact of the relative vertical distribution of dust and DIG shows that the DIG component needs to be accounted for in the models of Caplan & Deharveng (1986), Calzetti et al. (1994), and Wong & Blitz (2002). From our observations (Figures 6, 8 and 9) and simple models (Figures 10 and 11), we conclude that the differing scale heights of dust and gas in galaxies plays a large role in the measured extinction.

In general, we argue that the star-forming regions are born in a cocoon of dust, with the formed massive stars clearing the dust over time (Dreher & Welch 1981; Verley et al. 2010). The varying scale heights of dust and ionized gas (H II regions and DIG) with radius in galaxies can change the measured attenuation. At large galactocentric radii, especially in M31 with its low SFR, the H II regions remain embedded in their dusty cocoons that act as foreground screens. The DIG component is not as prominent in intensity or scale height. The DIG in M31 is well mixed with the thin dusty disk and additionally attenuated by the diffuse dust layer that acts as a screen. The high inclination of M31 also contributes to the higher attenuation.

On the other hand, in the more central and more active regions of galaxies (as in K13), the dust may be blown away by the numerous bright star-forming regions. The DIG will also be more prominent and extended, with a scale height larger than the scale height of dust. This leads to the DIG being less attenuated by dust and causing it to have a larger effect on observations of attenuation.

6. Summary

Using IFS and IR photometry in five 680 pc $\times$ 900 pc fields in M31, we explore the relative spatial distribution of dust and ionized gas. This is done at $\sim$100 pc scale resolution by comparing the attenuation (A_V) determined from the Balmer decrement and the dust mass surface density determined from fitting to the IR SED photometry (Σ_{dust}). We compare the results with two widely used theoretical models of the dust distribution (mixed and screen models, Calzetti et al. 1994) and with previous results from the literature for eight nearby galaxies (Kreckel et al. 2013, K13).

Our results show that the dust is approximately distributed as a uniform screen around the ionized gas in M31 (Figure 6). This is distinct from the galaxies observed by K13, which show attenuations between those predicted by the mixture of the foreground screen model and the mixed model (where the dust is uniformly mixed with the gas).

Variations in the spatial resolution do not appear to explain the differences in the measured attenuations (Figure 7).

The contribution from a small amount of non-attenuated gas emission in front of the dust disk can significantly lower the observed attenuation (Figure 8). This can lead to biases in observations of nearby galaxies. This additional gas can be associated with the DIG.

We also analyze the observed [S II]/Hα ratio and its correlation with A_V (Figure 9). Although our data do not show a clear trend, we found a difference in behavior between M31 and the nearby galaxies in K13. The M31 data show a slight increase of the ratio with A_V, while the K13 galaxies show the opposite trend.

Using two simple models, we explore the relationship between the observed line ratios and the relative spatial geometry of the dust, H II regions, and DIG gas (Figures 10 and 11). These models indicate that the relative vertical distribution and contribution of the DIG and the dust play a crucial role in changing the observed [S II]/Hα and A_V values at given values of the total dust column.

The difference in the results of M31 and K13 can be explained by the fact that the M31 fields lie at large galactocentric radii, whereas the K13 span fields that are in the centers of the galaxies. These differences in radii are associated with differences in the scale heights of the dust, DIG, and H II regions which impact the measured attenuation.

N.T. and K.K. acknowledge grants SCHI 536/8-2 and KR 4598/1-2 from the DFG Priority Program 1573. B.G. gratefully acknowledges the support of the Australian Research Council as the recipient of a Future Fellowship (FT140101202). G.B. is supported by CONICYT/FONDECYT, Programa de Iniciación, Folio 11150220.

We thank the anonymous referee for useful comments that helped to improve the paper. Furthermore, we thank I-Ting Ho (MPIA) for useful feedback and discussions, which also helped to improve the paper.

This work is based on observations collected at the Centro Astronòmico Hispano Alemàn (CAHA), operated jointly by the Max-Planck Institut für Astronomie and the Instituto de Astrofisica de Andalucia (CSIC), and is also based on observations made with *Herschel*. *Herschel* is an ESA space observatory with science instruments provided by European-led Principal Investigator consortia and with important participation from NASA. PACS has been developed by a consortium of institutes led by MPE (Germany) and including UVIE (Austria); KU Leuven, CSL, IMEC (Belgium); CEA, LAM (France); MPIA (Germany); INAF-IFSI/OAA/OAP/OAT, LENS, SISSA (Italy); and IAC (Spain). This development has been supported by the funding agencies BMVIT (Austria), ESA-PRODEX (Belgium), CEA/CNES (France), DLR (Germany), ASI/INAF (Italy), and CICYT/MCYT (Spain). SPIRE has been developed by a consortium of

institutes led by Cardiff University (UK) and including Univ. Lethbridge (Canada); NAOC (China); CEA, LAM (France); IFSI, Univ. Padua (Italy); IAC (Spain); Stockholm Observatory (Sweden); Imperial College London, RAL, UCL-MSSL, UKATC, Univ. Sussex (UK); and Caltech, JPL, NHSC, Univ. Colorado (USA). This development has been supported by national funding agencies: CSA (Canada); NAOC (China); CEA, CNES, CNRS (France); ASI (Italy); MCINN (Spain); SNSB (Sweden); STFC (UK); and NASA (USA). The work of A.K.L. is partially supported by the National Science Foundation under grants No. 1615105, 1615109, and 1653300.

Appendix A

The dust mass surface density maps used in this work were derived by the SED fitting method explained in Draine et al. (2014) and Groves et al. (2012), with an assumption of the Draine & Li (2007) dust model (here labeled as DL07). For details, see Section 2.

Two papers (Dalcanton et al. 2015; Planck Collaboration et al. 2016) recently tested the validity of the DL07 model by measuring the dust column density via extinction of the light from various background sources. Dalcanton et al. (2015) used the old stellar population in the thick disk of M31 for the light sources, while Planck Collaboration et al. (2016) used quasi-stellar objects (QSO) optical photometry. Both studies indicate a discrepancy by a factor of ∼2.5 between the DL07 estimates for A_V and A_V estimated from the background sources. Furthermore, comparison with independent FIR observations (*Planck*, *Herschel*, *Wise*, and *IRAS*) have shown that this offset is not due to uncertainties in the *Herschel* photometry (Verstappen et al. 2013; Planck Collaboration et al. 2016).

Planck Collaboration et al. (2016) propose an empirical renormalization of the dust mass derived from DL07 as a function of the DL07 ionization parameter U_{min} (see Formula 9 in Planck Collaboration et al. 2016). Figure 12 shows the A_V versus Σ_{dust} diagram for M31 and the nearby galaxies from K13, before and after using renormalization proposed by Planck Collaboration et al. (2016). The regions observed in K13 have $U_{min} > 1$. Because the renormalization is not calibrated in this high U_{min} regime, we do not include any renormalization of the K13 regions in this paper. However, extrapolating the renormalization would make Σ_{dust} of the K13 galaxies larger, thus widening the relative disagreement between M31 and K13.

The renormalized Σ_{dust} values for M31 are lower than before, pushing the values above the foreground screen limit lines. Given our confidence in our spectrophotometric calibration, we can only explain these relatively extreme A_V values as a result of either different physical dust properties or a non-uniform dust distribution (i.e., selective extinction of the H II regions). Such differences could lead to variations in extinction laws, DGR, and R_V.

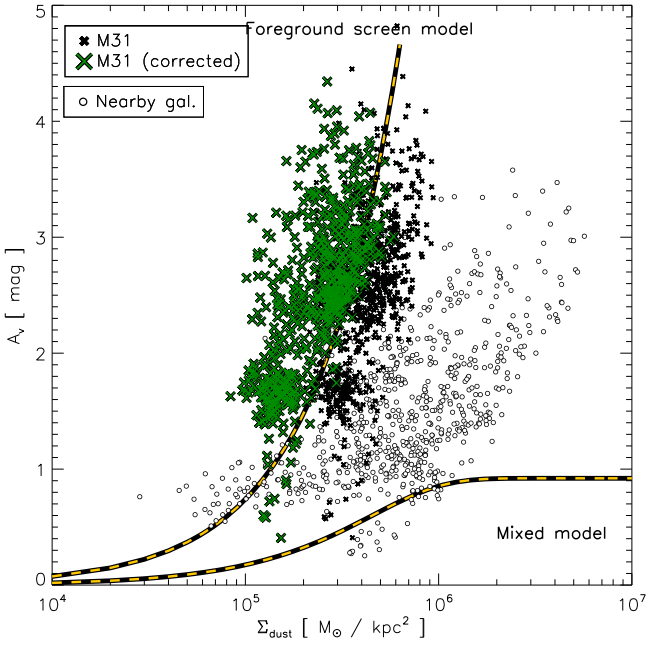

Figure 12. A_V vs. Σ_{dust} before and after correcting dust mass values using the empirically derived renormalization formula 9 in Planck Collaboration et al. (2016). Crosses indicate the data for M31 and circles the data for the nearby galaxies.

Appendix B

We investigate how the attenuation is affected by the different spatial resolutions between our M31 data and the nearby galaxy sample of K13. In Figure 13, we present A_V versus SFR density (Σ_{SFR}; from extinction corrected Hα) for both M31 and the K13 galaxies. The data points are color-coded base on Σ_{dust}. The K13 galaxies are at 0.3–2 kpc resolutions. We match our M31 data to the resolutions of K13 by integrating the fluxes in 0.6 kpc × 0.9 kpc fields. The lower resolution M31 data show significantly lower Σ_{SFR} than the K13 galaxies, making a direct comparison between M31 and the K13 galaxies at a fixed Σ_{SFR} impossible.

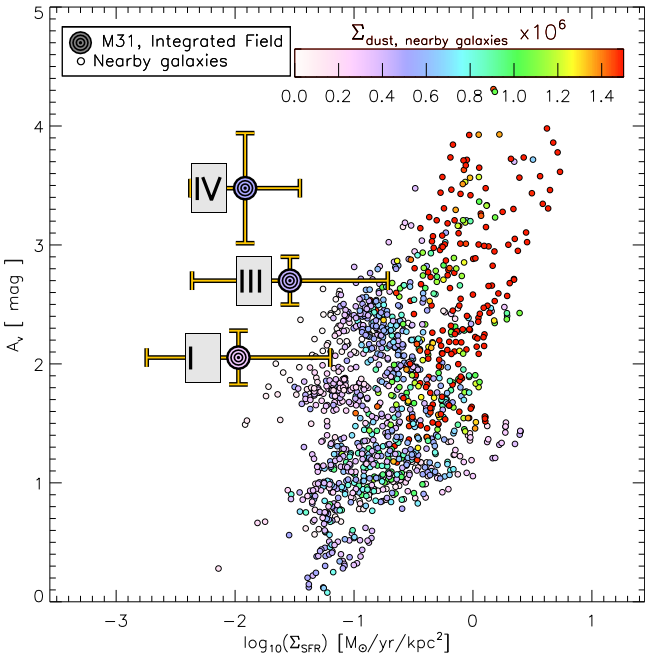

Figure 13. A_V vs. Σ_{SFR} (from extinction corrected Hα) of M31 (big circles) and K13 galaxies (small circles). Colors correspond to Σ_{dust} of the data. M31 data are at 0.6 kpc × 0.9 kpc resolution, while the K13 are at 0.3–2 kpc resolution.

References

Alton, P. B., Xilouris, E. M., Misiriotis, A., Dasyra, K. M., & Dumke, M. 2004, A&A, 425, 109
Aniano, G., Draine, B. T., Calzetti, D., et al. 2012, ApJ, 756, 138
Aniano, G., Draine, B. T., Gordon, K. D., & Sandstrom, K. 2011, PASP, 123, 1218
Ascasibar, Y., Guidi, G., Casado, J., Scannapieco, C., & Diaz, A. I. 2016, arXiv:1602.08474
Azimlu, M., Marciniak, R., & Barmby, P. 2011, AJ, 142, 139
Barnes, J. E., Wood, K., Hill, A. S., & Haffner, L. M. 2014, MNRAS, 440, 3027
Barnes, J. E., Wood, K., Hill, A. S., & Haffner, L. M. 2015, MNRAS, 447, 559
Bigiel, F., & Blitz, L. 2012, ApJ, 756, 183
Bigiel, F., Leroy, A., Seibert, M., et al. 2010, ApJL, 720, L31
Bishop, J., Mierkiewicz, E. J., Roesler, F. L., Gomez, J. F., & Morales, C. 2004, JGRA, 109, A05307
Bocchio, M., Bianchi, S., Hunt, L. K., & Schneider, R. 2016, A&A, 586, A8
Braun, R. 1991, ApJ, 372, 54
Bruzual, G., & Charlot, S. 2003, MNRAS, 344, 1000
Calzetti, D., Armus, L., Bohlin, R., et al. 2000, ApJ, 533, 682
Calzetti, D., Kinney, A. L., & Storchi-Bergmann, T. 1994, ApJ, 429, 582
Calzetti, D., Kinney, A. L., & Storchi-Bergmann, T. 1996, ApJ, 458, 132
Caplan, J., & Deharveng, L. 1986, A&A, 155, 297
Cappellari, M., & Emsellem, E. 2004, PASP, 116, 138
Cardelli, J. A., Clayton, G. C., & Mathis, J. S. 1989, ApJ, 345, 245
Collins, J. A., Rand, R. J., Duric, N., & Walterbos, R. A. M. 2000, ApJ, 536, 645
Dalcanton, J. J., Fouesneau, M., Hogg, D. W., et al. 2015, ApJ, 814, 3
Dalcanton, J. J., Williams, B. F., Lang, D., et al. 2012, ApJS, 200, 18
Dasyra, K. M., Xilouris, E. M., Misiriotis, A., & Klyafis, N. D. 2005, A&A, 437, 447
de Vaucouleurs, G., de Vaucouleurs, A., & Corwin, J. 1991, Third Reference Catalogue of Bright Galaxies Vol. I-III (New York: Springer)
Delaunay, B. 1934, Bulletin de l'Académie des Sciences de l'URSS, 6, 793
Dettmar, R.-J. 1990, A&A, 232, L15
Dettmar, R. J., & Schultz, H. 1992, A&A, 254, L25
Draine, B. T. 2011a, ApJ, 732, 100
Draine, B. T. 2011b, Physics of the Interstellar and Intergalactic Medium (Princeton, NJ: Princeton Univ. Press)
Draine, B. T., Aniano, G., Krause, O., et al. 2014, ApJ, 780, 172
Draine, B. T., & Li, A. 2007, ApJ, 657, 810
Dreher, J. W., & Welch, W. J. 1981, ApJ, 245, 857
Falcón-Barroso, J., Sánchez-Blázquez, P., Vazdekis, A., et al. 2011, A&A, 532, A95
Ferguson, A. M. N., Wyse, R. F. G., Gallagher, J. S., & Hunter, D. A. 1998, ApJL, 506, L19
Ferguson, A. M. N., Wyse, R. F. G., Gallagher, J. S., III, & Hunter, D. A. 1996, AJ, 111, 2265
Galametz, M., Kennicutt, R. C., Albrecht, M., et al. 2012, MNRAS, 425, 763
García-Burillo, S., Combes, F., & Neri, R. 1999, A&A, 343, 740
Gordon, K. D., Clayton, G. C., Misselt, K. A., Landolt, A. U., & Wolff, M. J. 2003, ApJ, 594, 279
Greenawalt, B., Walterbos, R. A. M., Thilker, D., & Hoopes, C. G. 1998, ApJ, 506, 135
Griffin, M. J., Abergel, A., Abreu, A., et al. 2010, A&A, 518, L3
Groves, B., Krause, O., Sandstrom, K., et al. 2012, MNRAS, 426, 892
Groves, B. A., & Allen, M. G. 2010, NewA, 15, 614
Haffner, L. M., Dettmar, R. J., Beckman, J. E., et al. 2009, RvMP, 81, 969
Haffner, L. M., Reynolds, R. J., Tufte, S. L., et al. 2003, ApJS, 149, 405
Heald, G. H., Rand, R. J., Benjamin, R. A., & Bershady, M. A. 2006, ApJ, 647, 1018
Holwerda, B. W., Bianchi, S., Böker, T., et al. 2012, A&A, 541, L5
Holwerda, B. W., & Keel, W. C. 2013, A&A, 556, A42
Horne, K. 1986, PASP, 98, 609
Howk, J. C. 2012, EAS, 56, 291
Hughes, T. M., Baes, M., Fritz, J., et al. 2014, A&A, 565, A4
Kapala, M. J., Sandstrom, K., Groves, B., et al. 2015, ApJ, 798, 24
Kennicutt, R. C., Calzetti, D., Aniano, G., et al. 2011, PASP, 123, 1347
Kewley, L. J., Groves, B., Kauffmann, G., & Heckman, T. 2006, MNRAS, 372, 961
Koyama, H., & Ostriker, E. C. 2009, ApJ, 693, 1346
Kreckel, K., Armus, L., Groves, B., et al. 2014, ApJ, 790, 26
Kreckel, K., Groves, B., Schinnerer, E., et al. 2013, ApJ, 771, 62
Lewis, A. R., Dolphin, A. E., Dalcanton, J. J., et al. 2015, ApJ, 805, 183
Liu, G., Calzetti, D., Hong, S., et al. 2013, ApJL, 778, L41
Madsen, G. J., Reynolds, R. J., & Haffner, L. M. 2006, ApJ, 652, 401
Matthews, L. D., & Wood, K. 2003, ApJ, 593, 721
Miller, J. S. 1974, ARA&A, 12, 331
Minter, A., & Balser, D. S. 1998, LNP, 506, 543
Neugebauer, G., Habing, H. J., van Duinen, R., et al. 1984, ApJL, 278, L1
Nossal, S., Roesler, F. L., & Bishop, J. 2001, JGR, 106, 5605
O'Brien, J. C., Freeman, K. C., & van der Kruit, P. C. 2010, A&A, 515, A63
Oey, M. S., Meurer, G. R., Yelda, S., et al. 2007, ApJ, 661, 801
Oke, J. B. 1990, AJ, 99, 1621
Olling, R. P. 1996, AJ, 112, 457
Osterbrock, D. E. 1974, Astrophysics of Gaseous Nebulae (San Francisco, CA: W.H. Freeman & Co.)
Osterbrock, D. E., & Martel, A. 1992, PASP, 104, 76
Osterbrock, D. E., & Martel, A. 2006, Mercu, 35, 40
Pety, J., Schinnerer, E., Leroy, A. K., et al. 2013, ApJ, 779, 43
Pilbratt, G. L., Riedinger, J. R., Passvogel, T., et al. 2010, A&A, 518, 1
Planck Collaboration, Ade, P. A. R., Aghanim, N., et al. 2016, A&A, 586, A132
Popescu, C. C., Tuffs, R. J., Dopita, M. A., et al. 2011, A&A, 527, A109
Rand, R. J. 1996, ApJ, 462, 712
Rand, R. J. 1998, ApJ, 501, 137
Rand, R. J. 2005, in ASP Conf. Ser. 331, Extra-Planar Gas, ed. R. Braun (San Francisco, CA: ASP), 163
Reach, W. T. 1997, in ASP Conf. Ser. 124, Diffuse Infrared Radiation and the IRTS, ed. H. Okuda, T. Matsumoto, & T. Rollig (San Francisco, CA: ASP), 33
Regan, M. W., Thornley, M. D., Vogel, S. N., et al. 2006, ApJ, 652, 1112
Reynolds, R. J. 1971, BAAS, 3, 17
Reynolds, R. J. 1984, ApJ, 282, 191
Reynolds, R. J. 1990, in The Galactic and Extragalactic Background Radiation (Dordrecht: Kluwer Academic Publishers), 157
Reynolds, R. J., & Cox, D. P. 1992, ApJL, 400, L33
Roth, M. M., Kelz, A., & Fechner, T. 2005, PASP, 117, 620
Rupen, M. P. 1991, AJ, 102, 48
Sánchez, S. F. 2006, AN, 327, 850
Sánchez-Blázquez, P., Peletier, R. F., & Jiménez-Vicente, J. 2006, MNRAS, 371, 703
Sancisi, R., & Allen, R. J. 1979, A&A, 74, 73
Sanders, N. E., & Caldwell, N. M. J. H. P. 2012, ApJ, 758, 133
Sandin, T., Becker, M., Roth, M. M., et al. 2010, A&A, 515, A35
Sarzi, M., Falcón-Barroso, J., & Davies, R. L. 2006, MNRAS, 366, 1151
Schlafly, E. F., & Finkbeiner, D. P. 2011, ApJ, 737, 103
Schlegel, D. J., Finkbeiner, D. P., & Davis, M. 1998, ApJ, 500, 525
Schultz, G. V., & Wiemer, W. 1975, A&A, 43, 133
Scoville, N. Z., Thakkar, D., Carlstrom, J. E., & Sargent, A. I. 1993, ApJL, 404, L59
Slanger, T. G., Huestis, D. L., & Cosby, P. C. 2000, JCP, 113, 8514
Stanek, K. Z., & Garnavich, P. M. 1998, ApJL, 503, L131
Tempel, E., Tuvikene, T., Tamm, A., & Tenjes, P. 2011, A&A, 526, A155
Tremonti, C. A., Heckman, T. M., & Kauffmann, G. 2004, ApJ, 613, 898
Tyler, K., Quillen, A. C., & LaPage, A. 2004, ApJ, 610, 213
van der Hulst, J. M., Kennicutt, R. C., Crane, P. C., & Rots, A. H. 1988, A&A, 195, 38
van Dokkum, P. G. 2001, PASP, 113, 1420
Velusamy, T., & Langer, W. D. 2014, A&A, 572, A45
Verheijen, M., Bershady, M., & Andersen, D. 2004, AN, 325, 151
Verley, S., Relaño, M., Kramer, C., et al. 2010, A&A, 518, L68
Verstappen, J., Fritz, J., Baes, M., et al. 2013, A&A, 556, A54
Viaene, S., Baes, M., Tamm, A., et al. 2017, A&A, 599, A64
Walterbos, R. A. M., & Braun, R. 1994, ApJ, 431, 156
Wang, J., Heckman, T. M., & Lehnert, M. D. 1999, ApJ, 515, 97
Williams, B. F. 2003, AJ, 126, 1312
Witt, A. N., Thronson, H. A., Jr., & Capuano, J. M., Jr. 1992, ApJ, 393, 611
Wong, T., & Blitz, L. 2002, ApJ, 569, 157
Wynn-Williams, C. G. 1982, ARA&A, 20, 587
Yasui, K., Nishiyama, S., & Yoshikawa, T. 2015, PASJ, 67, 123
Yim, K., Wong, T., Xue, R., et al. 2014, AJ, 148, 127
York, D. G., Adelman, J., & Anderson, J. E., Jr. 2000, AJ, 120, 1579
Zschaechner, L. K., & Rand, R. J. 2015, ApJ, 808, 153
Zurita, A., & Bresolin, F. 2012, MNRAS, 427, 1463